Published for SISSA by Springer

Received: July 25, 2022
Accepted: September 12, 2022
Published: October 4, 2022

Ultra-relativistic bubbles from the simplest Higgs portal and their cosmological consequences

Aleksandr Azatov,[a,b,c] **Giulio Barni,**[a,b] **Sabyasachi Chakraborty,**[a,b,c] **Miguel Vanvlasselaer**[a,b,c] **and Wen Yin**[d]

[a] *SISSA International School for Advanced Studies, Via Bonomea 265, 34136, Trieste, Italy*
[b] *INFN — Sezione di Trieste, Via Bonomea 265, 34136, Trieste, Italy*
[c] *IFPU, Institute for Fundamental Physics of the Universe, Via Beirut 2, 34014 Trieste, Italy*
[d] *Department of Physics, Tohoku University, Sendai, Miyagi 980-8578, Japan*

E-mail: aleksandr.azatov@sissa.it, giulio.barni@sissa.it, sachakr@sissa.it, miguel.vanvlasselaer@sissa.it, yin.wen.b3@tohoku.ac.jp

Abstract: We analyze phase transitions in the minimal extension of the SM with a real singlet scalar field. The novelty of our study is that we identify and analyze in detail the region of parameter space where the first order phase transition can occur and in particular when the bubbles with true vacuum can reach relativistic velocities. This region is interesting since it can lead to the new recently discussed baryogenesis and Dark Matter production mechanisms. We fully analyze different models for the production of Dark Matter and baryogenesis as well as the possibilities of discovery at the current and future experiments.

Keywords: Baryon/Lepton Number Violation, Cosmology of Theories BSM

ArXiv ePrint: 2207.02230

https://doi.org/10.1007/JHEP10(2022)017

JHEP10(2022)017

Contents

JHEP10(2022)017

1 Introduction

The origin of Dark Matter (DM) and matter antimatter asymmetry are one of the most important unresolved puzzles of the early Universe cosmology. In this paper we will investigate in detail the novel mechanisms proposed in [1–3] for DM production and baryon asymmetry generation during the first order phase transitions (FOPT).

The FOPT are known to be very useful for constructing baryogenesis models since the process is out-of-equilibrium as required by one of the Sakharov's conditions [4]. Applications of this mechanism to the electroweak phase transition lead to the seminal scenarios of electroweak baryogenesis [5, 6]. In the Standard Model (SM), electroweak phase transition is expected to be a smooth crossover [7, 8]. However, this is not the case for various Beyond Standard Model (BSM) frameworks where successful scenarios of electroweak baryogenesis can be built (see for a recent review [9]). The connection between DM and phase transitions is less direct. However, there are class of models where these two phenomenon are strongly related (see for example refs. [10–30]).

The focus of this paper will be electroweak FOPT with very relativistic bubbles. In this context, collision between bubbles and particles in the plasma, as was shown recently [31], can lead to the production of new states with mass scale significantly larger than the scale of the phase transition.[1] These heavy states can serve as DM candidates [2] or their production and subsequent decay [1, 3], if accompanied with C, CP and baryon number violating interactions can lead to baryon asymmetry generation. The successful realization of this scenario require bubble expansion with ultra-relativistic velocities. Such bubble wall motion is known to be possible and is expected within certain classes of the potentials ([33–37]). However in the case of electroweak phase transition, the requirement of ultra relativistic velocities leads to very non-trivial constraints on the effective potential. In this paper we analyze in detail the simplest extension of the SM that can lead to a FOPT: real singlet scalar field. There have been numerous studies of phase transition in this type of scenario [38–48]. The Lagrangian can be restricted further by considering Z_2 [49] or Z_3 symmetries [50, 51]. Interestingly such a real singlet scalar field can appear in composite Higgs models [52] (see also [53–55] for studies pertaining to phase transition). However, most of the above mentioned works did not analyze in detail the region of parameter space with relativistic bubbles since slow bubble wall velocities are required [5, 6] for the usual electroweak baryogenesis. We fill this gap by analyzing in detail phase transitions in the real singlet extension of SM with an approximate Z_2 discrete symmetry, focusing on the parameter space which results in very fast bubble expansions. Anticipating the results of this paper we found that the most promising scenario for relativistic bubbles is the case where the phase transition occurs in two steps: the first transition is related to the Z_2 symmetry breaking while keeping EW symmetry unbroken and in the second one the Higgs field acquires its vacuum expectation value (vev) which comes together with Z_2 symmetry restoration.

[1] Note that this effect is different from the mechanism presented in [25, 32] where the heavy fields are produced by the collisions between different bubble walls.

JHEP10(2022)017

This will permit us to evaluate the region of parameter space where Baryogenesis via relativistic bubble walls is viable and to put constraints on the mass scale of the dark sector responsible for CP and B violation. Implications for non-thermal DM production from bubble wall plasma particle collisions will also be considered.

The article is organised as follows: in section 2, we review the singlet extension of the SM and write the two fields potential with thermal corrections. In section 3, we remind the reader of the basics of FOPTs in early Universe and present the computation of the terminal velocity of the bubble wall in the ultra-relativistic regime, for the generic case and for SM. In section 4, we qualitatively discuss the different patterns of phase transitions and argue that only a two-steps PT can yield ultra relativistic bubble wall motion. In section 5 we present a numerical study of the two-steps PT analyzing in detail the region with fast bubble motion. In section 6, we draw the consequences of our previous results for the production of heavy DM and Baryogenesis and in section 7, we comment on the GW signal induced by such strong transitions. Finally, in section 8, we summarize and conclude.

2 Review of the singlet extension of the SM

Let us start by reviewing the effective potential of the SM with a real scalar field (s). The scalar potential will be given by

$$V(\mathcal{H}, s) = -\frac{m_h^2}{2}(\mathcal{H}^\dagger\mathcal{H}) + \lambda(\mathcal{H}^\dagger\mathcal{H})^2 - \frac{m_s^2}{4}s^2 + \frac{\lambda_{hs}}{2}s^2(\mathcal{H}^\dagger\mathcal{H}) + \frac{\lambda_s}{4}s^4\,, \tag{2.1}$$

where $\mathcal{H}$ is the SM Higgs doublet and $m_h \approx 125\,\text{GeV}$ is the physical mass of the Higgs. For simplicity, we will impose Z_2 symmetry on the potential to avoid the terms with odd powers of s field. As a result, when $\langle s\rangle = 0$, we avoid any scalar mixing terms which are constrained by the recent Higgs signal strength measurements [56]. The Higgs doublet can be decomposed as usual

$$\mathcal{H}^T = \left(G^+, \frac{h + iG^0}{\sqrt{2}}\right), \tag{2.2}$$

where h is the usual Higgs boson getting a vev which is given by $v_{EW} = \sqrt{m_h^2/2\lambda} \approx 246\,\text{GeV}$ if $\langle s\rangle \equiv v_s = 0$.

2.1 Coleman-Weinberg potential

Next, we take into account 1-loop corrections which are encapsulated by the Coleman-Weinberg (CW) potential [57]

$$V_{CW} = \sum_{i=Z,h,W,t} \frac{n_i(-1)^F}{64\pi^2}\left[M_i^4\left(\log\frac{M_i^2}{M_{i0}^2} - \frac{3}{2}\right) + 2M_i^2M_{i0}^2\right]. \tag{2.3}$$

In this expression, M_i stand for the masses depending on the Higgs and singlet fields values, $M_i \equiv M_i(h, s)$, and M_{i0} are the field values from the tree-level vev, $M_{i0} \equiv M_i(v_{EW}, 0)$.

JHEP10(2022)017

Then one can easily check that this potential corresponds to the following renormalization conditions

$$V_{\rm eff} = V_0 + V_{CW},$$
$$\left.\frac{dV_{\rm eff}}{dh}\right|_{(h,s)=(v_{EW},0)} = 0, \qquad \left.\frac{d^2V_{\rm eff}}{dh^2}\right|_{(h,s)=(v_{EW},0)} = m_h^2\,. \tag{2.4}$$

Eq. (2.3) cannot be used directly for contributions of the Goldstone bosons, since their masses vanish in the true vacuum and the CW potential is IR divergent. However the solution to this issue was suggested in ref. [58] which emphasized that the physical Higgs mass is defined at $p^2 = m_h^2$ and the effective potential at $p^2 = 0$ (see for details ref. [58]). Thus it would be better to use modified renormalization condition

$$\left.\frac{d^2V_{\rm eff}}{dh^2}\right|_{(h,s)=(v_{EW},0)} = m_h^2 - \Sigma\left(p^2 = m_h^2\right) + \Sigma\left(0\right)\,, \tag{2.5}$$

where the differences of self-energies are taking into account the running of self-energy from $p^2 = 0$ to $p^2 = m_h^2$. In this case the IR divergences in $\Sigma(0)$ due to the virtual Goldstone bosons are cancelled against the IR divergences of $V_{\rm eff}$. In practice, at the end of this renormalization procedure, the contribution of the Goldstone bosons is given by:

$$V_{CW}^{GB}(h) = \sum_{i=G}\frac{n_G}{64\pi^2}M_{G^{\pm},0}^4(h)\left[\log\frac{M_G^2}{m_h^2} - \frac{3}{2}\right]. \tag{2.6}$$

The number of d.o.f, masses of various particles and the scalar mass matrix as functions of h, s are given by:

$$n_{W^\pm} = 6, \qquad n_Z = 3, \qquad n_{G^{\pm},0} = 3, \qquad n_t = 12\,,$$
$$M_{W^\pm}^2(h) = \frac{g^2h^2}{4}, \quad M_Z^2(h) = \frac{g^2+g'^2}{4}h^2, \quad M_{G^{\pm},0}^2(h) = -\frac{m_h^2}{2} + \lambda h^2, \quad M_t^2(h) = \frac{y_t^2h^2}{2}$$
$$M^2(h,s) = \begin{pmatrix} 3\lambda h^2 + \frac{\lambda_{hs}}{2}s^2 - \frac{m_h^2}{2} & \lambda_{hs}sh \\ \lambda_{hs}sh & 3\lambda_s s^2 + \frac{\lambda_{hs}}{2}h^2 - \frac{m_s^2}{2} \end{pmatrix}. \tag{2.7}$$

As a side remark, in the region where the Higgs $h \to 0$ and $s \sim O(v_{EW})$, there will be two scales involved in the problem: the value of the singlet field s and the masses of the SM particles $M_{W,Z,t}(h \to 0, s) \to 0 \ll s$. This type of two scale potential has been studied in the past [59], by using two different renormalisation scales. It was concluded that resummation is needed when the $\log\left(M_i(0,s)/s\right)$ is large enough to cancel the loop suppression. Although we have two largely separated scales, we have checked that for our region of the parameter space, such a resummation is not necessary.

2.2 Finite temperature potential

The temperature and the density effects can be taken into account by complementing the zero temperature potential with thermal corrections (see for example [60, 61]),

$$V(T, M_i) = V_{\rm eff}^{T=0}(M_i) + V_T(M_i)\,. \tag{2.8}$$

JHEP10(2022)017

In eq. (2.8), $V_{\rm eff}^{T=0}(M_i)$ is the potential we computed in the previous subsection and the thermal potential $V_T(M_i)$ is given by

$$V_T(M_i(h,s)) = \sum_{i\in B}\frac{n_i}{2\pi^2}T^4 J_B\left(\frac{M_i^2(h,s)}{T^2}\right) - \sum_{i\in F}\frac{n_i}{2\pi^2}T^4 J_F\left(\frac{M_i^2(h,s)}{T^2}\right),$$
$$J_{B/F}(y^2) = \int_0^\infty dx\; x^2 \log\left[1 \mp \exp\left(-\sqrt{x^2+y^2}\right)\right]. \tag{2.9}$$

However, to save computation time, we use the approximate expansion of the function $J_{B/F}(y^2)$ as given in ref. [60]:

$$J_B(y^2) = \begin{cases} -\frac{\pi^4}{45} + \frac{\pi^2}{12}y^2 - \frac{\pi}{6}y^3 - \frac{y^4}{32}\log\left[\frac{y^2}{16\pi^2\exp[3/2-2\gamma]}\right], & y^2 \ll 1\,, \\ -\sum_{n=1}^{m>3}\frac{1}{n^2}y^2 K_2(yn)\,, & y^2 \gg 1\,, \end{cases}$$
$$J_F(y^2) = \begin{cases} \frac{7\pi^4}{360} - \frac{\pi^2}{24}y^2 - \frac{y^4}{32}\log\left[\frac{y^2}{\pi^2\exp[3/2-2\gamma]}\right], & y^2 \ll 1\,, \\ -\sum_{n=1}^{m>3}\frac{(-1)^n}{n^2}y^2 K_2(yn)\,, & y^2 \gg 1\,. \end{cases} \tag{2.10}$$

where $\gamma \approx 0.577$ is the *Euler constant*, and $K_2(z)$ are the second-kind Bessel function. To account for dangerously divergent higher loops due to the Daisy diagrams at finite temperature, we follow the so-called "Truncated-Full-Dressing" procedure [60].[2] Doing so, the full one-loop potential becomes

$$V(h,s,T) = V_{\rm tree}(h,s) + \sum_i \left[V_{CW}\left(M_i^2(h,s)+\Pi_i(h,T)\right) + V_T\left(M_i^2(h,s)+\Pi_i(h,T)\right)\right], \tag{2.11}$$

where $\Pi_i(T)$ are the thermal masses of various degrees of freedom. In the real singlet extension of the SM [60], the expressions of the thermal masses read

$$\text{Scalar:}\quad \Pi_h(T) = T^2\left(\frac{3g^2}{16} + \frac{g'^2}{16} + \frac{\lambda}{2} + \frac{y_t^2}{4} + \frac{\lambda_{hs}}{24}\right), \quad \Pi_s(T) = T^2\left(\frac{\lambda_{hs}}{6} + \frac{\lambda_s}{4}\right), \tag{2.12}$$

$$\text{Gauge:}\quad \Pi_g^L(T) = T^2\,\text{diag}\left(\frac{11}{6}g^2, \frac{11}{6}(g^2+g'^2)\right), \qquad \Pi_g^T(T) = 0\,, \tag{2.13}$$

where $\Pi_g^L(T)$ denote the thermal mass of the *longitudinal* mode of the gauge bosons, while transverse modes $\Pi_g^T(T)$ are protected by gauge invariance and thus do not receive a mass at leading order in perturbation theory.

3 First order phase transitions with relativistic bubbles

Starting with the effective potential derived in the previous section, we can proceed to the analysis of the phase transition. FOPT happens when the minima of the potential

[2] Recently for the singlet scalar extensions of the SM have been proposed more sophisticated method for computing the thermal potential with two loop dimensional reduction to the three dimensional effective field theory see [62, 63].

JHEP10(2022)017

corresponding to different phases are separated by a potential barrier and the transition happens via bubble nucleation. The probability of nucleation of a bubble is given by [64–66]

$$\Gamma(T) \simeq \Gamma_3 + \Gamma_4 = T^4 \left(\frac{S_3}{2\pi T}\right)^{3/2} e^{-S_3(T)/T} + \frac{1}{R_0^4}\left(\frac{S_4}{2\pi}\right) e^{-S_4}\,, \tag{3.1}$$

where S_3, S_4 are $O(3,4)$ bounce actions and R_0 is the initial bubble radius. Bubble nucleation is characterised by a critical temperature $T_{\rm crit}$, defined as the point when the two phases of the system have vacua with the same energy. Below $T_{\rm crit}$ phase transition becomes energetically possible. The probability to find a specific point of the Universe to be in the false vacuum is given by [36, 67, 68]:

$$P_f[T] = \exp[-I(T)]\,, \qquad I(T) \equiv \frac{4\pi}{3}\int_T^{T_c} \frac{dT_1 \Gamma(T_1) v_w^3}{T_1^4 H(T_1)} \left[\int_T^{T_1} \frac{dT_2}{H(T_2)}\right]^3. \tag{3.2}$$

In eq. (3.1) the strongest dependence on the temperature comes from the $\Gamma(T) \propto \exp\left(-S_3/T\right)$, so that the quantity $I(T)$ is mostly controlled by the ratio $\Gamma\left(T\right)/H^4\left(T\right)$ and an order one fraction of the volume of the Universe will be in the true vacuum when $\Gamma[T] \sim H^4[T]$. The temperature that satisfies this condition is coined as the nucleation temperature $T_{\rm nuc}$ or, to phrase differently, the nucleation temperature $T_{\rm nuc}$ corresponds to the appearance of roughly one bubble of true vacuum per Hubble volume. Assuming the scale of the phase transition to be $O(100)$ GeV we get

$$\Gamma \sim H^4, \qquad H(T)^2 = \frac{1}{3M_{\rm pl}^2}\left(\rho_{\rm rad} + \rho_{\rm vac} + \rho_{\rm wall}\right), \quad \rho_w \approx 0, \quad \rho_{\rm rad} = \frac{\pi^2 g_\star}{30} T^4, \tag{3.3}$$

$$\rho_{\rm vac} = \Delta V, \quad \Rightarrow \quad \frac{S_3}{T_{\rm nuc}} = \frac{3}{2}\log\left(\frac{S_3}{2\pi T_{\rm nuc}}\right) + 4\log\left(\frac{T_{\rm nuc}}{H}\right). \tag{3.4}$$

In case we want to be more precise about the temperature when the phase transition completes, we can define the so-called *percolation temperature* $T_{\rm per}$ as the temperature when around ∼30 % of the space has been converted to the true phase

$$I(T \equiv T_{\rm per}) = 0.34\,, \qquad \text{(percolation temperature)}. \tag{3.5}$$

If the condition in eq. (3.5) is not fulfilled, $I(T) < 0.34$, then the bubbles do not percolate.

At last the energy released during the PT is traditionally quantified by the ratio between the energy stored in the vacuum and in the plasma at the moment of the transition

$$\alpha \equiv \frac{\Delta V}{\rho_{\rm rad}} \qquad \text{(strength parameter)}. \tag{3.6}$$

3.1 Velocity of the EW bubble

Let us proceed to the computation of the bubble wall velocity v_w. The dynamics of the bubble wall motion is controlled by the driving force due to the potential differences between the false and true vacuum

$$\Delta V \equiv V_{\rm false} - V_{\rm true}\,, \tag{3.7}$$

JHEP10(2022)017

and the friction due to finite temperature effects. The calculation of the friction is generically a very complicated problem, however for the ultra-relativistic bubble motion at leading order (LO - tree level) very simple expressions have been obtained [69, 70] for the pressure force from friction,

$$\Delta\mathcal{P}_{\rm LO} \simeq \sum_i g_i c_i \frac{\Delta M_i^2}{24} T_{\rm nuc}^2 \,, \tag{3.8}$$

where ΔM_i^2 is the change in the mass of the particle i during the PT, $c_i = 1\,(1/2)$ for bosons (fermions) and g_i is the number of d.o.f of the incoming particle. Eq. (3.8) assumes that the masses of the particles outside of the bubble are less than the temperature, otherwise the friction will have an additional Boltzmann suppression $\propto \exp[-M_{\rm false}/T]$. Interestingly the production of the heavy particles can also contribute to the friction at the same order [31]

$$\Delta\mathcal{P}_{\rm LO}^{\rm mixing} \propto v^2 T^2 \Theta(\gamma_w T_{\rm nuc} - M_{\rm heavy}^2/v) \,, \tag{3.9}$$

where v is the vev of the Higgs field and we review the heavy particle production later in the section 6.1. One can see that the friction (pressure from plasma on the bubble wall) becomes velocity independent so that permanent accelerating (runaway) behavior of the bubble expansion becomes possible. However for theories where the gauge bosons receive a mass during the phase transition, this is not the case and the effect with multiple gauge boson emissions, leads to the additional contribution (NLO- Next to Leading order) to the pressure which scales as [20, 31, 71, 72][3]

$$\Delta\mathcal{P}_{\rm NLO} \propto \sum_a g_a g_{\rm gauge}^3 \gamma_w T_{\rm nuc}^3 v \,. \tag{3.10}$$

At this point we can see that bubbles will keep accelerating till the moment when NLO friction becomes large enough to balance the driving force

$$\Delta V = \Delta\mathcal{P}_{\rm LO} + \Delta\mathcal{P}_{\rm LO}^{\rm mixing} + \Delta\mathcal{P}_{\rm NLO}, \tag{3.11}$$

which will set the $\gamma_w^{\rm terminal}$ the bubble can reach,

$$\gamma_w^{\rm terminal} \sim \left(\frac{\Delta V - \Delta\mathcal{P}_{\rm LO} - \Delta\mathcal{P}_{\rm LO}^{\rm mixing}}{T_{\rm nuc}^3 v} \right). \tag{3.12}$$

Note that we can be as well in the situation where the percolation (bubble collision) starts before the terminal $\gamma_w^{\rm terminal}$ is reached.

3.2 Friction forces during the electroweak phase transitions

Let us apply the discussion of the previous section to the EW phase transition (EWPT). Our main interest will be the possibility of heavy particle production which can later source baryogenesis and DM production following the ideas in [1–3, 31]. The heavy particle production (see also the discussion in section 6.1) happens due to the collision between the plasma particles and the bubble wall. The typical center of mass energy for such process

[3] There is a claim that this friction scales as $\gamma^2 T^4$ [73] see [31, 72] for criticism.

JHEP10(2022)017

will be roughly $\sim \sqrt{\gamma_w T v_{EW}}$, thus γ_w will be controlling the maximal mass of the new fields that can be produced. To calculate γ_w in the context of the EWPT, we need to know the forces acting on the bubble wall.

The LO friction from the top, Z, and W takes the form:

$$\Delta\mathcal{P}^{SM}_{\rm LO} \approx T^2_{\rm nuc} v^2_{EW}\left(\frac{y_t^2}{8}+\frac{g^2+g'^2}{32}+\frac{g^2}{16}\right)\approx 0.17\, T^2_{\rm nuc} v^2_{EW}. \tag{3.13}$$

There is also a contribution to the LO friction from the singlet and Higgs scalars, however it depends on the masses of these fields in the false vacuum and we find it to be numerically subleading compared to the estimate in eq. (3.13).[4] In our numerical calculation we took this additional contribution into account, however, for the current discussion it is sufficient to use eq. (3.13). This gives a rough condition on the nucleation temperature for the transition to become ultra-relativistic

$$\Delta V > 0.17\, T^2_{\rm nuc} v^2_{EW} \qquad \text{(relativistic wall condition)}. \tag{3.14}$$

The computation of the NLO friction in the SM has been carried out in [72] and the following approximate expression has been derived:

$$\Delta\mathcal{P}^{SM}_{\rm NLO} \approx \left[\sum_{abc}\nu_a g_a \beta_c C_{abc}\right]\frac{\kappa\zeta(3)}{\pi^3}\alpha M_Z(v_{EW})\gamma_w \log\frac{M_Z(v_{EW})}{\mu} T^3_{\rm nuc}\,, \tag{3.15}$$

where $\nu_a = 1(3/4)$ for a a boson (fermion), g_a is the number of degrees of freedom of a and $M_{g,i}(v_{EW})$ is the mass of the gauge boson inside the bubble. C_{abc} represents the coupling which appears in the vertex (see appendix C), $\beta_{c=Z^0} = 1$, and $\beta_{c=W^\pm} = \cos\theta_W = M_W/M_Z$, $\alpha = e^2(v_{EW})/4\pi \sim 1/128$ is the electromagnetic fine structure constant. The renormalization scale μ has to be understood as the lower cut-off for the integration over soft momentum, typically the thermal mass $\mu \propto \alpha_i^{1/2} T_{\rm nuc}$ [31]. The κ factor is introduced [72] to account for the contributions of the both reflected and transmitted bosons and is approximately equal to $\kappa \sim 4$. The sum in the square brackets is approximately equal to

$$\left[\sum_{abc}\nu_a g_a \beta_c C_{abc}\right] \approx 157\,, \tag{3.16}$$

see appendix C for details. At this point we can compute the terminal wall velocity by balancing the pressure against the driving force

$$\Delta V - \Delta\mathcal{P}^{SM}_{\rm LO} = \Delta\mathcal{P}^{SM}_{\rm NLO}(\gamma_w = \gamma_w^{\rm terminal}) \quad \text{(Terminal velocity criterion)} \tag{3.17}$$

$$\Rightarrow \gamma_\omega^{\rm terminal} \sim 6\times\left(\frac{\Delta V - \Delta\mathcal{P}^{SM}_{\rm LO}}{(100\text{ GeV})^4}\right)\left(\frac{100\text{GeV}}{T_{\rm nuc}}\right)^3 \frac{1}{\log(M_Z/gT_{\rm nuc})}. \tag{3.18}$$

Taking into account that $(\Delta V - \Delta\mathcal{P}_{\rm LO})/(100\text{ GeV})^4 \lesssim \mathcal{O}(1)$, we can see that the bubbles will become ultra-relativistic, i.e. $\gamma^{\rm terminal} \gg 1$ only if $T_{\rm nuc}$ is significantly lower than the scale of the phase transition $\sim 100\,$GeV.

[4] These contributions are smaller due to the number of d.o.f. and possible Boltzmann suppression factors $\propto \exp[-M_{\rm false}/T]$.

JHEP10(2022)017

4 Phase transition in the singlet extension

After the preparatory discussion in the previous sections 2 and 3, we can proceed to the analysis of phase transition in the model with the singlet field, eq. (2.1). Our analysis will be focused on the region of parameter space with relativistic bubble expansion, for other studies of phase transition in SM plus Z_2 real singlet scalar, see refs. [49, 74–76].

In the previous section 3, we have seen that the velocity of the bubble expansion is fixed by the balance between the friction from the plasma and the driving force. At low temperatures the friction is suppressed (see eq. (3.13)–(3.15)) so that we expect the bubbles to become relativistic (large Lorentz $\gamma_w^{\rm terminal}$ factor).

Let us check whether low nucleation temperatures are feasible in the singlet extension. We will assume that Z_2 remains unbroken in the true vacuum in order to avoid to constraints from the Higgs-scalar mixing (see for example [77]). Then in the model with Z_2 odd singlet, the phase transition can occur in two ways: one-step $(\langle h\rangle = 0, \langle s\rangle = 0) \to (v_{EW}, 0)$ and two-steps[5] $(\langle h\rangle = 0, \langle s\rangle = 0) \to (0, \langle s\rangle|_{\neq 0}) \to (v_{EW}, 0)$ [46, 49, 75], and each of these phase transitions can be first or the second order. We review both of these scenarios of phase transitions in order to understand in what case it is possible to obtain relativistic bubbles.

4.1 One-step phase transition

This case has been largely studied in the literature [49, 75] and we will not provide a complete description of it. In this scenario the singlet never gets a vev, and all of its effect reduce to the additional contributions to the Higgs potential from Coleman-Weinberg terms and thermal corrections. However it turns out that relativistic bubbles are very unlikely for such phase transitions (see also results in [49]). In the limit when $|m_s| \ll T_{\rm crit}$ we can show analytically that this is indeed the case. Near the origin $h \to 0$, the potential in h direction is dominated by the $\propto h^2$ terms

$$V_{\rm dominant}(h \to 0, s = 0, T) = \frac{m^2_{\rm eff}(T)}{2} h^2 + \dots \tag{4.1}$$

The effective mass $m^2_{\rm eff}$ include the tree-level terms and the leading thermal contributions and is approximately equal to

$$m^2_{\rm eff}(T) \simeq -m_h^2 + T^2 \left(\frac{m_h^2}{4 v_{EW}^2} + \frac{y_t^2}{4} + \frac{g^2 + g'^2}{16} + \frac{g^2}{8} + \frac{\lambda_{hs}}{24} \right) > 0\,. \tag{4.2}$$

The FOPT can happen only if $m^2_{\rm eff}(T) > 0$. Then assuming perturbative values of the coupling λ_{hs} we can estimate the lowest temperature where the FOPT can occur to be $T^{nuc}_{\rm min} \gtrsim 100\,{\rm GeV}$. Comparing this value with the discussion in the section 3.2 we can see that the bubble wall velocities will always satisfy $\gamma_w \lesssim 10$. As mentioned before, we are interested in the expansions with much larger γ_w factors, so that we do not discuss one step phase transition further.

[5] We will see later that at temperatures $T \ll T_c$ Coleman-Weinberg potential can shift a little bit the false vacuum position to $(\delta v_h, v_s)$ where $\delta v_h \ll v_s, v_h$.

JHEP10(2022)017

4.2 Two step FOPT with relativistic bubbles

Two-steps realisations of the EWPT have already been studied in many works, see for example [46, 49, 75, 78–82]. The novelty of our study is that we will be focusing on the parameter space with relativistic bubbles which was previously ignored. We organize the discussion as follows: in section 4.2, we show qualitative results based on approximate treatment of the potential and then in the section 5 we present the exact numerical results obtained with our code. The two-steps phase transition

$$(0,0) \to (0,\langle s\rangle) \to (v_{EW},0)\,, \tag{4.3}$$

can happen if the m_s^2 parameter of eq. (2.1) is positive. In this case it is convenient to parameterize the Lagrangian in the following way

$$V_{\rm tree}(h,s) = -\frac{m_h^2}{4}h^2 + \frac{m_h^2}{8v_{EW}^2}h^4 - \frac{m_s^2}{4}s^2 + \frac{\lambda_{hs}}{4}s^2h^2 + \frac{m_s^2}{8v_s^2}s^4\,. \tag{4.4}$$

where $v_{EW} = \sqrt{m_h^2/2\lambda}\,\text{GeV}$ and $v_s = \sqrt{m_s^2/2\lambda_s}$ correspond to the local minima at $(\langle h\rangle = v_{EW}, \langle s\rangle = 0)$ and $(\langle h\rangle = 0, \langle s\rangle = v_s)$ respectively. The origin of two-steps PT can be intuitively understood from the following considerations. For simplicity let us ignore the Coleman-Weinberg potential and restrict the discussion by considering only the thermal masses. Then the potential will be given by

$$\begin{aligned} V(\mathcal{H},s) &\approx V_{\rm tree}(\mathcal{H},s) + \frac{T^2}{24}\left[\sum_{bosons} n_i M_i^2(\mathcal{H},s)) + \frac{1}{2}\sum_{fermions} n_F M_F^2(\mathcal{H},s)\right]\,, \\ &= V_{\rm tree}(\mathcal{H},s) \\ &\quad + T^2\left[h^2\left(\frac{g'^2}{32} + \frac{3g^2}{32} + \frac{m_h^2}{8v_{EW}^2} + \frac{y_t^2}{8} + \frac{\lambda_{hs}}{48}\right) + s^2\left(\frac{m_s^2}{16v_s^2} + \frac{\lambda_{hs}}{12}\right)\right]. \end{aligned} \tag{4.5}$$

From this expression we can clearly see that the temperatures when the minima with non zero vevs appear for the Higgs and singlet fields can be different. Then it can happen that the Z_2 breaking phase transition occurs before the EW one. This means that there will be first a phase transition from $(0,0) \to (0,v_s)$. After this phase transition the Universe keeps cooling down and the minimum with $\langle h\rangle \neq 0$ will be generated. Choosing the appropriate values of masses and couplings we can make sure that the minimum with $(v_{EW},0)$ is the true minimum of the system. The transition $(0,v_s) \to (v_{EW},0)$ will be of the first order if there is a potential barrier between the two minima. One of the necessary condition in this case will be $\partial^2 V/\partial h^2|_{s=v_s,h\to 0} > 0$, which using eq. (4.5) we get

$$\frac{-m_h^2}{4} + \frac{\lambda_{hs}v_s^2}{4} + T^2\left(\frac{g'^2}{32} + \frac{3g^2}{32} + \frac{m_h^2}{8v^2} + \frac{y_t^2}{8} + \frac{\lambda_{hs}}{48}\right) > 0\,. \tag{4.6}$$

From this discussion we can see that there are qualitatively two different cases depending on whether the potential barrier between two minima remains or disappears at zero

JHEP10(2022)017

temperature, i.e. when $m_h^2 \gtrless \lambda_{hs} v_s^2$. In the first case the phase transition will necessarily happen before the "No Barrier"(NB) temperature

$$T^{\rm NB} = \sqrt{\frac{m_h^2 - \lambda_{hs} v_s^2}{\frac{g'^2}{8} + \frac{3g^2}{8} + \frac{m_h^2}{2v^2} + \frac{y_t^2}{2} + \frac{\lambda_{hs}}{12}}} \sim \frac{v_s \sqrt{-\lambda_{hs} + \left(\frac{m_h}{v_s}\right)^2}}{0.8}\,, \tag{4.7}$$

since the bounce action drops once the potential barrier between two minima reduces.

In the other case, when the barrier remains even for zero temperature potential, the phase transition is obviously of the first order. However it might happen that the tunneling rate is too slow and the system remains stuck in the false vacuum.

From eq. (4.6) we can see that the size of the potential barrier between the two minima is controlled by the coupling λ_{hs}. Increasing this parameter will enhance the potential barrier and will lead to the reduction of $T^{\rm NB}$ so that $(v_s, 0)$ remains a local minimum even at zero temperature. At some point we expect the potential barrier to become so large that the system will remain trapped in the false vacuum forever. From this discussion we can expect that the lowest temperatures will be achieved at the boundary of the region where no PT can occur. The lowest temperature will correspond to the (global) minimum of S_3/T controlling the tunneling rate, as explained later in section 5. If this minimum happens at temperatures much lower than $T_{\rm crit}$, then there will be super-cooling ($T_{\rm nuc} \ll T_{\rm crit}$). Even though this discussion was made by considering only the thermal masses in the potential, numerically we find that for the effective potential with truncated full dressing [60] the qualitative behaviour does not change, and only explicit conditions for m_h^2 and $T_{\rm min}^{\rm nuc}$ are modified.

At last we always check whether the condition for the EWSB minimum to be the global minimum at zero temperature is satisfied:

$$m_s^2 v_s^2 < m_h^2 v_{EW}^2 \qquad \text{(EWSB is global minimum)}\,, \tag{4.8}$$

where above equation is valid up to small loop-level corrections.

5 Numerical results

After the qualitative discussion, let us proceed to the numerical calculations. The bounce action for $(0, v_s) \to (v_{EW}, 0)$ was computed using our own dedicated code (cross checked against `FindBounce` [83]) and we relegate the details and methods of this calculation to appendix A. We parameterize our model in terms of (m_s, λ_{hs}, v_s) parameters (see eq. (4.4)). Instead of analyzing all the possible values of m_s, in this section we report the results (see figure 1 left panel) by fixing $m_s = 125\,\text{GeV}$ (there is no particular reason for this value of m_s and the results for the other values of m_s are similar and are shown in the appendix B). In the plane (see figure 1) $v_s - \lambda_{hs}$, we identify four regions with different behaviours under the phase transition. The blue region shows second order transition when there is no barrier between the two separated vacuum. Next to it there is a light red region where the transition is of the first order. We indicate separately (dark red) the region, where the transition is of the first order and the bubbles are relativistic. In particular the boundary

JHEP10(2022)017

between the regions with relativistic and non-relativistic bubbles is defined by the criteria of eq. (3.14), i.e. when the LO pressure for relativistically expanding bubbles is less than the driving force. At last, there is NO PT region, where the system remains stuck in the false vacuum since the tunnelling rate is too small.

The structure of the diagram (on the figure 1 top−left panel) can be easily understood from the qualitative discussion in the previous section. Indeed, keeping v_s fixed, the size the potential barrier is controlled by the coupling λ_{hs}. Moving from left to right the size of the potential barrier increases and we are gradually moving from the region of second order phase transition → FOPT → FOPT with relativistic bubbles → no PT region. Similarly moving up (increasing v_s for fixed values of λ_{hs}) also corresponds to the increase of the potential barrier as we pass though the regions with different PT in the same order. On the upper axis we report physical mass of the singlet in the true vacuum $M_s(v_{EW}, 0)$ and exclude the constrained region where $h \to ss$ is kinematically allowed (the gray meshed region).

Next we plot the values of $T_{\rm nuc}$ and $\gamma_w^{\rm terminal}$ as a function of (λ_{hs}, v_s) (figure 1). As discussed in the previous section, the region with the smallest values of the nucleation temperature (thus the fastest bubbles) is located near the "NO PT" region, i.e. where the system remains trapped in the false vacuum. The blue dot on the $T_{\rm nuc}$ plot indicates the last point we have found before the system enters the regime of no phase transition (NO PT). In the bottom right we plot $M_{\rm max} = \sqrt{\gamma_w T_{\rm nuc} v_{EW}}$ quantity which indicates the maximal energy in the c.o.m frame for the plasma particle−bubble wall collision, which corresponds to the largest mass of the heavy particles we can produce (see discussion in section 6.1).

In order to better understand the dependencies of $T_{\rm nuc}$ and γ_w on the parameters of the model, it is useful to separate further the parameter space depending on whether the potential barrier disappears at zero temperature or not. This is important since the bounce action in such cases has very different dependencies on the temperature. See for example figure 2, where we have plotted the S_3/T for $v_s = 170\,\text{GeV}$, $m_s = 125\,\text{GeV}$ for the various couplings λ_{hs}. In the case when the potential barrier disappears at some temperature $T^{\rm NB}$ the function S_3/T drops to zero, but if the barrier remains even at zero temperature S_3/T has a global minimum for $T \neq 0$ which will be controlling the lowest nucleation temperature possible.

5.1 No potential barrier at zero temperature

Let us start by defining the region where there is no potential barrier at zero temperature. On figure 1, we demonstrate the curves where the barrier disappears for various values of the temperatures ($T^{\rm NB}$). For $T^{\rm NB} = 0$ case, approximate curve can be obtained analytically by looking at the leading terms in the zero temperature CW potential

$$\lambda_{hs} \lesssim \frac{m_h^2}{v_s^2} - \frac{n_t y_t^4}{32\pi^2}\frac{v_{EW}^2}{v_s^2}\,. \tag{5.1}$$

The agreement between this equation and exact $T^{\rm NB} = 0$ curve is at the level of a few permille discrepancies. To the right of $T^{\rm NB} = 0$ curve, the potential barrier between the

JHEP10(2022)017

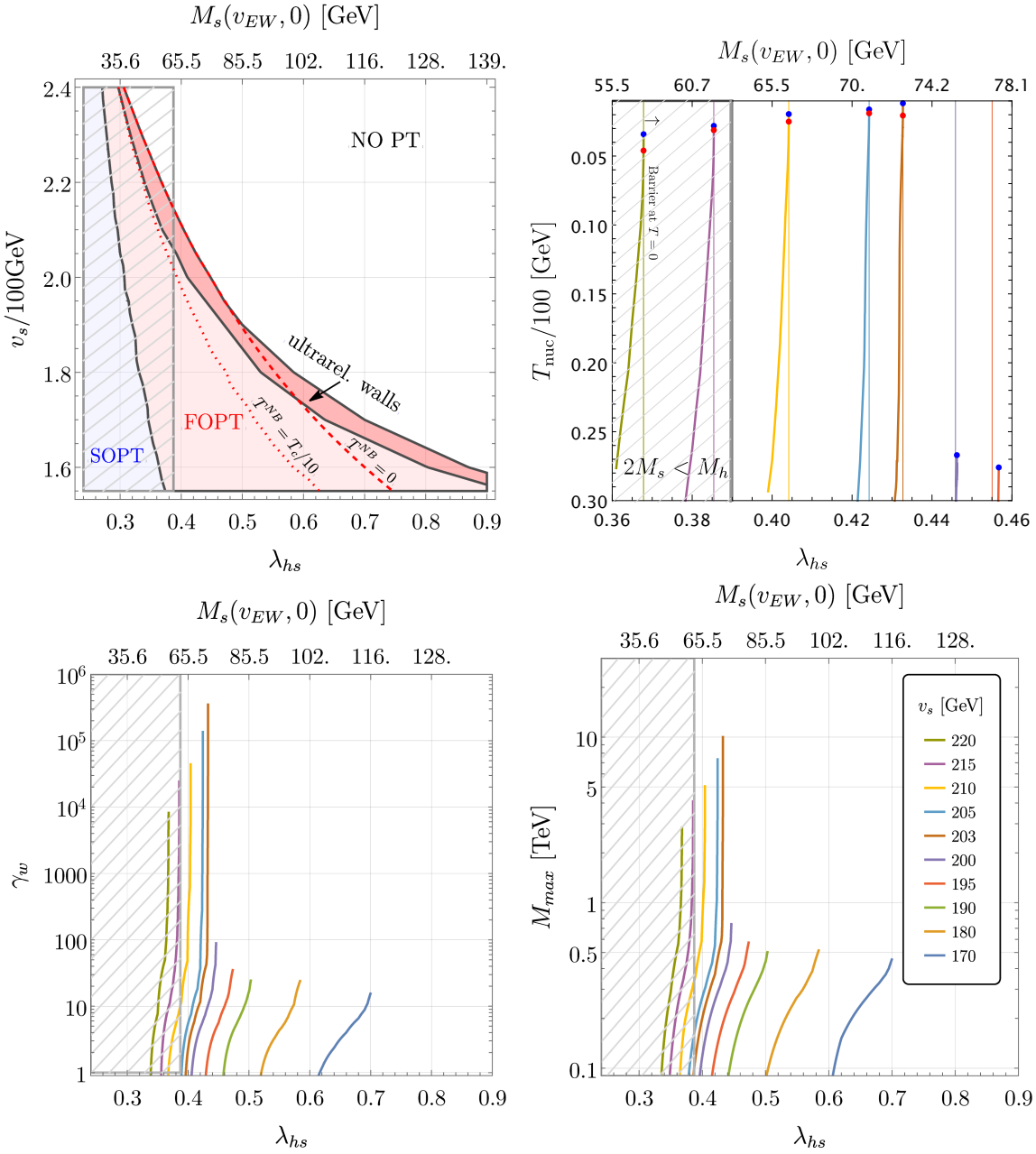

Figure 1. **Top-Left**: scan of the parameter space in the plane $\lambda_{hs} - v_s$ for $m_s = 125\,\text{GeV}$. The four regions are as follows: i) white - NO PT, the region where the transition never completes because the barrier remains at zero temperature and the function S_3/T never passes below the nucleation condition, ii) light and dark red are the regions where the FOPT happens. Dark (light) red corresponds to the region with relativistic (non-relativistic) bubble expansion. The boundary between two regions is given by eq. (3.14) iv) blue - the phase transition is of the second order. The gray meshed region is the one in which $M_s(v_{EW},0) < m_h/2$, that is constrained from collider experiments. **Top-Right and Bottom**: the dependencies of $T_{\rm nuc}, \gamma_w,\ M_{\rm max}$ on the λ_{hs} coupling for $m_s = 125\,\text{GeV}$. The blue dot on the Top-Right plot designates the end of the curve, when the tuning becomes 10^{-6} and the red dot signals the appearance of a barrier at zero temperature (all the points above the red dot have a barrier at $T = 0$). For the last three plots we varied the λ_{hs} parameter with the steps of 10^{-6}. The value of v_s is encoded in color according to the bottom-right plot.

JHEP10(2022)017

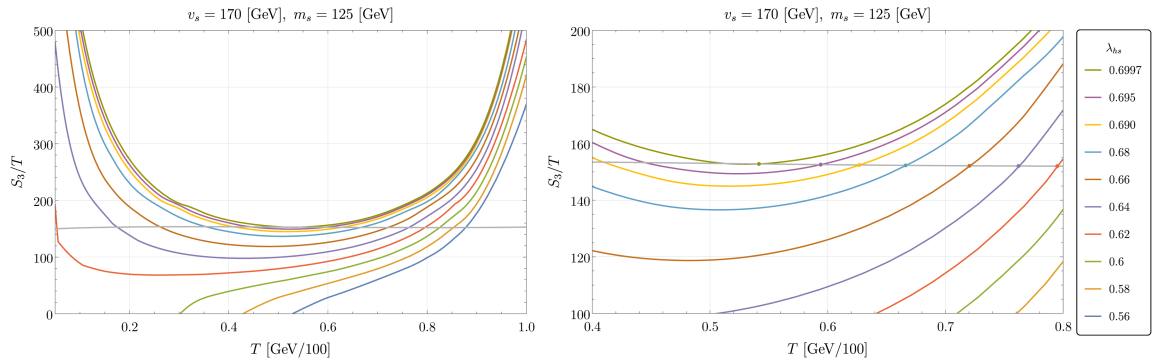

Figure 2. **Left**: S_3/T function with $v_s = 170\,\text{GeV}$ and $m_s = 125\,\text{GeV}$. We observe that the nucleation temperature saturates around $T_{\text{nuc}} \approx 54\,\text{GeV}$. The horizontal gray line satisfy the nucleation condition $S_3/T_{\text{nuc}} = \frac{3}{2}\log\left(S_3/2\pi T_{\text{nuc}}\right) + 4\log\left(T_{\text{nuc}}/H\right)$. **Right**: zooming in on the region with lower nucleation temperatures.

two minima remains even at zero temperatures. For the values $v_s \gtrsim 200\,\text{GeV}$, we find that the line $T^{\text{NB}} = 0$ approximately coincides with the boundary of no phase transition region (where system remains stuck in the false vacuum) but obviously the boundary of "NO PT" is always to the right of $T^{\text{NB}} = 0$ curve. The size of this narrow strip is of the order 10^{-4} in λ_{hs} values. One can see it from the T_{nuc} panel of figure 1 where we have indicated the value of λ_{hs} when $T_{\text{NB}} = 0$ by vertical thin line and red dot (for intersection) and the position of the blue dot which is the last point where the transition is of the first order before we enter NO PT region. The boundaries of this region were obtained by numerical calculations where we have scanned λ_{hs} parameter with a step 10^{-6}. We postpone the discussion of the FOPT in this narrow region to the next section 5.2.

In this section we restrict our discussion only on the region to the left of $T^{\text{NB}} = 0$ curve. Then the phase transition will be always completed before the universe cools down to T^{NB}, i.e. $T^{\text{NB}} < T_{\text{nuc}}$, which provides a lower bound for the nucleation temperature. At the same time the velocity of the bubbles become largest for the smallest possible values for the nucleation temperature. So that the fastest bubbles will be near $T^{\text{NB}} = 0$ curve. Looking at figure 1 we can see that the largest γ_w (Lorentz boost factor) and lowest nucleation temperatures happen for $v_s \gtrsim 200\,\text{GeV}$, where the $T^{\text{NB}} = 0$ curve passes very close to the NO PT boundary. The shape of the lines in figure 1 clearly indicates the necessity of tuning in order to obtain low nucleation temperatures (large γ_w). In particular for the values of $v_s \gtrsim 200\,\text{GeV}$ we can see that the nucleation temperature drops by choosing λ_{hs} close to the NB value (similarly γ_w becomes maximal see figure 1). We can estimate this tuning by looking at $\partial \log \lambda_{hs}/\partial \log T_{\text{nuc}}$ quantity (analogue of Giudice-Barbieri [84] measure of the tuning) as a function of T_{nuc}. This result agrees with our expectation from the steepness of the curves in the figure 3 and with the naive tuning expectation which scales as $\sim \left(T_{\text{nuc}}/m_h\right)^2$.[6]

At last we would like to remind that the discussion in this section always assumed that

[6]This expression follows eq. (4.6) if we require the cancellation between the terms independent of temperature.

JHEP10(2022)017

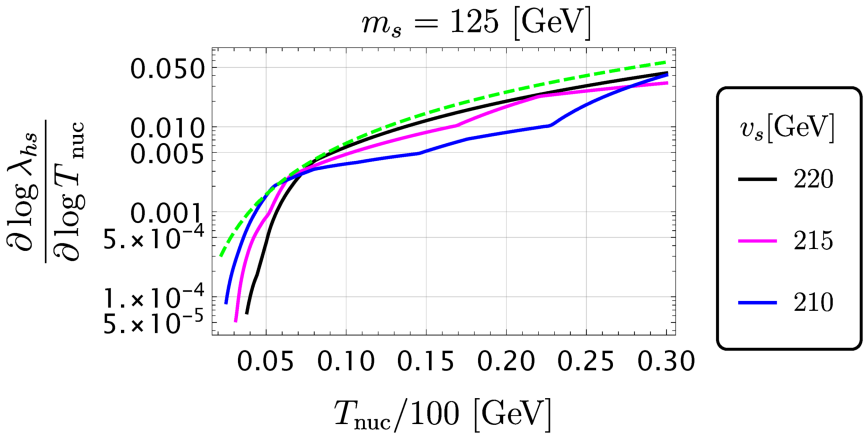

Figure 3. Tuning of the coupling λ_{hs} as a function of the nucleation temperature. The dashed green line represents the naive tuning $\sim (T_{\rm nuc}/m_h)^2$. We observe that this naive estimation for the tuning is rather precise at large nucleation temperature but can underestimate the tuning by one order of magnitude for very low nucleation temperature.

the phase transition completes before the potential barrier disappears. We have checked numerically that this is always the case. Indeed the time of the phase transition is given approximately by the bubble radius at the moment of percolation [85, 86]

$$R_\star \equiv \frac{(8\pi)^{1/3}}{\tilde{\beta}} = \left(\int_{T_{\rm per}}^{T_{\rm crit}} \frac{dT}{T} \frac{\Gamma(T)}{H(T)} \left(\frac{T_{\rm per}}{T} \right)^3 \right)^{-1/3} . \tag{5.2}$$

This radius is related to the $\beta \equiv -\frac{d}{dt}\frac{S_3}{T} = HT\frac{d}{dT}\frac{S_3}{T}$ parameter by an approximate relation [86]

$$\left.\frac{\beta}{H}\right|_{T_{\rm per}} \simeq \frac{\tilde{\beta}}{H} = \frac{(8\pi)^{1/3}}{R_\star H} , \tag{5.3}$$

where we find $R_\star^{-1} \sim \beta_{\rm typical} \sim (10 - 10^4)H$.

At this point the temperature drop during the bubble expansion will scale as

$$\Delta T \sim T_{\rm nuc}(H\Delta t) \sim \frac{T_{\rm nuc} H}{\beta} . \tag{5.4}$$

Due to the large value of β/H we find numerically that this drop of the temperature is not enough for the barrier to disappear or in other words

$$T_{\rm nuc} - \Delta T > T^{\rm NB} . \tag{5.5}$$

Such behaviour can be understood from the following consideration: near $T_{\rm NB}$ the bounce action drops very quickly and so that the tunneling becomes very efficient almost instantaneous and typical bubble radiuses are much smaller than the Hubble scale. This leads to another prediction that GW signal will be suppressed as well since it is controlled by the (β/H) quantity eq. (5.3). As we will see, even with this suppression the GW signal is efficient enough to be detected in the future.

JHEP10(2022)017

5.2 Tunneling with potential barrier at zero temperature

Let us proceed to the analysis of the case when the potential barrier does not disappear at zero temperature. The parameter space with the lowest nucleation temperatures (fastest bubbles) will be located again near the "NO PT" boundary. However in this case the nucleation temperature will be controlled by the local minima of the S_3/T function, see figure 2. At least a minimum is expected since the potential at low temperature becomes fully temperature independent and $S_3(T \to 0) \to$ const., so that S_3/T necessarily starts to grow for $T \to 0$.

Numerically (see figure 1) for the value of $m_s = 125\,\text{GeV}$ we find that for $v_s \lesssim 170\,\text{GeV}$ entire region with the fast bubbles has a potential barrier at zero temperature. On figure 2, we present the euclidean action for $v_s = 170\,\text{GeV}$ and $m_s = 125\,\text{GeV}$. Going back to figure 1, we see that for those values the "NO PT" curve and the "$T_{\text{NB}} = 0$" curve are largely separated. This is not a surprise since in this region of parameter space the bounce action $S_3/T \sim O(10^2)$ is small enough to guarantee the successful tunneling even when the barrier remains at zero temperature. In the range of λ_{hs} from 0.5 to 0.7, numerically we find that nucleation temperatures are $\gtrsim 30\,\text{GeV}$, and the corresponding maximal Lorentz factors for the velocities of the bubble expansion in the ranges of $\lesssim 30$, see table 1. Interestingly we find that in this case the bubble radius $R_\star \sim \frac{(8\pi)^{1/3} v_w}{\beta}$ are a little bit larger than the ones discussed in the section 5.1, corresponding to a bit smaller values of β/H parameter.

Super fine-tuned region. We finally comment on the parameter space with $v_s \gtrsim 200\,\text{GeV}$ (again we are fixing $m_s = 125\,\text{GeV}$), where the curves "NO PT" and "$T_{\text{NB}} = 0$" almost superimpose (the region between red and blue dots on the T_{nuc} panel of the figure 1). There will be a very narrow strip between the curves "NO PT" and "$T_{\text{NB}} = 0$" regions, where the tunnelling will happen even though the barrier remains at zero temperature. We find (see figure 4) that the region corresponds to the variations of the λ_{hs} parameter of the order $\delta\lambda_{hs} \sim O(10^{-4})$, i.e. two order of magnitude smaller than the full region with relativistic bubbles. In this very small region various additional effects can start playing a role. For example let us look at the figure 4 we can see that the bounce action S_3/T has a local maximum and a deeper (global) minimum with respect to the standard scenario. Such a behaviour of the action is coming from the cancellations of various terms in the effective potential. For simplicity let us look at $T = 0$ case. Then there is a region of parameter space where purely polynomial potential has no local minimum at $(0, v_s)$, but the effects of the $\frac{-3M_t^4(h)}{8\pi^2}\left(\log \frac{M_t(h)}{M_t(v_{EW})}\right)$ terms in Coleman-Weinberg contribution lead to the appearance of the local minimum at $(\delta v_h, v_s)$. On figure 5 we plot the contributions of the various terms in the effective potential leading to the appearance of this local minimum and the trajectory of the typical bounce solution in this case. As a result the distance in the fields space between the two minima decreases and the tunneling becomes faster, which leads to the appearance of the second (global) minimum in S_3/T.

5.2.1 Benchmark points

In table 1 and 2, we give typical values of the nucleation temperature, the Lorentz factor γ_w, the β/H factor, and we indicate if the barrier remains at zero temperature, applying

JHEP10(2022)017

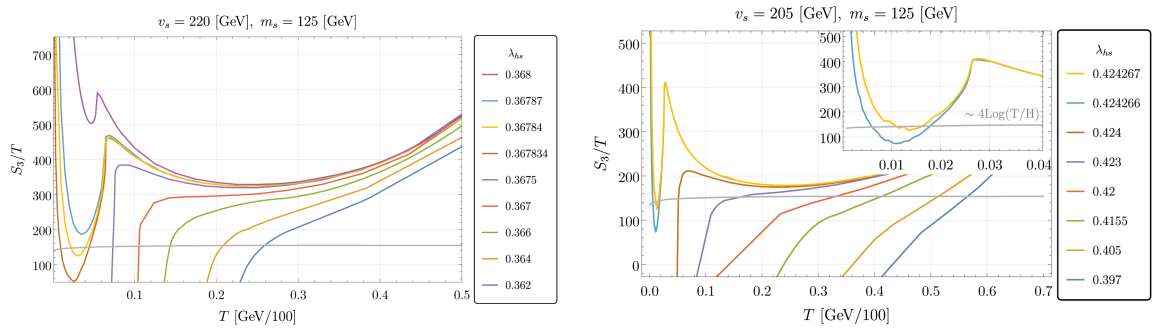

Figure 4. **Left**: plot of $S_3(T)/T$ as a function of the temperature, for different values of λ_{hs} in the case where $m_s = 125\,\text{GeV}$ and $v_s = 220\,\text{GeV}$. As we increase the value of the coupling λ_{hs}, the disappearance of the potential barrier happens later, allowing for longer supercooling, until it is large enough to remain even at zero temperature. For the first four curves from the top, we observe a second drop in the function at very low temperature. This second drop corresponds to the displacement on the false minimum that we describe in this section. **Right**: same plot as in the left panel, but with a lower value for v_s. The pattern we found is the same, but lowering v_s causes a lowering of the curves and the displacement of the false minimum is less pronounced.

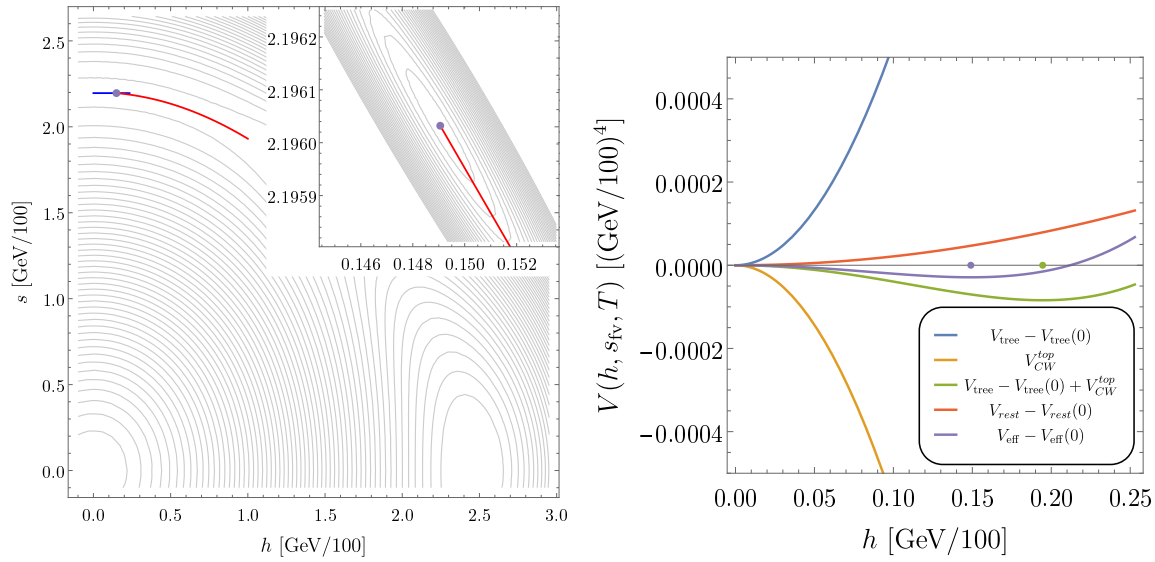

Figure 5. Here is presented an explicit example of displacement of the false vacuum for $\{\lambda_{hs}, v_s, T\} = \{0.36784, 220\ \text{GeV}, 3\ \text{GeV}\}$. **Left**: we show the 2D potential where the blue line corresponds to the part of the potential plotted in the right panel and the (purple) dot is the position of the displaced false minimum, in both the plots. Red line indicates the bounce trajectory. **Right**: plot of the different contributions to the potential. We see that a displaced minimum can be generated balancing the tree level and the CW potential of the top quark, for low enough temperature, in such a way all the other particles, that are massless in the false vacuum, have a negligible contribution. It can be shown that they cause, as the temperature increases, the shift of the local minimum towards $h = 0$.

JHEP10(2022)017

$m_s = 125\,\text{GeV}, \quad v_s = 170\,\text{GeV}$							
λ_{hs}	$\frac{T_{\text{reh}}}{100\text{GeV}}$	$\frac{T_{\text{nuc}}}{100\text{GeV}}$	$\frac{T_{\text{per}}}{100\text{GeV}}$	γ_w	$\frac{\tilde{\beta}}{H} = \frac{(8\pi)^{1/3}}{R_\star H}$	$m_H^{\text{False}}/\text{GeV}$	FM_0
0.56	0.880	0.877	0.850	–	434	35.4	No
0.58	0.855	0.851	0.822	–	355	37.3	No
0.6	0.829	0.824	0.790	–	296	39.2	No
0.62	0.800	0.795	0.762	1.2	209	40.1	No
0.64	0.769	0.762	0.714	2.4	158	42.5	No
0.66	0.729	0.720	0.661	4	108	43.4	No
0.68	0.678	0.666	0.582	6.6	51	44.8	No
0.69	0.642	0.627	0.506	8.8	18	45.0	No
0.695	0.612	0.594	0.412	11	5	44.7	No
0.6997	0.566	0.542	0.237	15	1.4	43.8	No

Table 1. We report for figure 2, $m_s = 125\,\text{GeV}$ and $v_s = 170\,\text{GeV}$, reheating, nucleation and percolation temperatures, respectively, for different values of λ_{hs} and γ_w reached by the expanding walls as well as the parameter $\tilde{\beta}/H$ computed using eq. (5.3). We also show the effective Higgs mass in the false vacuum at the nucleation temperature defined as $(m_H^{\text{False}})^2 = \frac{\partial^2 V}{\partial h^2}\big|_{T=T_{\text{nuc}}}$, relevant for DM production explained in section 6.2. In the last column, FM_0 concerns the displacement of the false minimum. No if it is at the (Higgs) origin, yes if it moved. In this case, the minimum is always at the origin.

$m_s = 125\,\text{GeV}, \quad v_s = 205\,\text{GeV}$							
λ_{hs}	$\frac{T_{\text{reh}}}{100\text{GeV}}$	$\frac{T_{\text{nuc}}}{100\text{GeV}}$	$\frac{T_{\text{per}}}{100\text{GeV}}$	γ_w	$\frac{\tilde{\beta}}{H} = \frac{(8\pi)^{1/3}}{R_\star H}$	$m_H^{\text{False}}/\text{GeV}$	FM_0
0.397	0.577	0.564	0.544	4	371	19.1	No
0.405	0.530	0.512	0.488	8	268	19.1	No
0.4155	0.448	0.412	0.379	18	130	17.7	No
0.42	0.393	0.330	0.290	37	72	15.2	No
0.423	0.339	0.161	0.124	270	66	7.1	No
0.4234	0.335	0.107	0.095	805	109	3.9	No
0.424	0.335	0.051	0.051	$5.7 \cdot 10^3$	$3.3 \cdot 10^3$	0.7	No
0.4242	0.335	0.0337	0.0337	$1.8 \cdot 10^4$	$3.2 \cdot 10^4$	0.25	No
0.42424	0.335	0.028	0.0279	$3.0 \cdot 10^4$	$1.8 \cdot 10^3$	4.4	No
0.424266	0.335	0.018	0.017	$1.0 \cdot 10^5$	99	6.2	Yes
0.424267	0.335	0.016	0.014	$1.3 \cdot 10^5$	44	6.3	Yes

Table 2. Same as table 1, but for figure 4 and with $v_s = 205\,\text{GeV}$. We observe that the last two points display a displacement of the false minimum.

the criterion in eq. (5.5). We can see that the largest bubble radius at the collision (smallest β) correspond to the case when S_3/T is monotonic and very flat near the tunneling temperature (cf. the right panel of figure 4).

JHEP10(2022)017

6 Consequences for production of dark matter and Baryogenesis

One of the motivation for the study of a model of EWPT with relativistic bubbles is the relation between relativistic expansion and the out-of-equilibrium production of heavy states presented for the first time in [31], when the field undergoing the PT (here the Higgs) is coupled to some heavy dark sector of typical mass M_N. In this section, we remind the principle of the production mechanism and we study the scenario of the production of Dark Matter [2] and Baryogenesis [1], that were previously agnostic about the EWPT realisation.

First of all, the strong FOPT involves a supercooling represented by a dilution factor,

$$D \equiv \frac{g_{\star s}^{\rm sym}(T_{\rm nuc})}{g_{\star s}(T_{\rm reh})} \left(\frac{T_{\rm nuc}}{T_{\rm reh}}\right)^3 , \tag{6.1}$$

with $g_{\star s}(T)$ ($g_{\star s}^{\rm sym}(T)$) being the number of relativistic degrees of freedom of the entropy in the broken (symmetric) phase. This means that with $D \ll 1$, any type of dark matter production or Baryogenesis mechanism that happens much earlier than the PT should provide values denser than the conventional estimation by a factor of $1/D$ (see for example [19, 87]). For instance, the WIMP cross section should be $\sigma \sim \frac{D}{10^{-3}} 10^{-29} {\rm cm}^3/{\rm s}$ to produce a correct dark matter abundance. This is the case when freeze-out happens at temperatures much higher than the reheating.

6.1 Production of heavy states during ultra-relativistic expansion

There are few mechanisms which can lead to heavy particle production during FOPT. This can happen if the incoming massless particle in the unbroken phase gets a very large mass from the Higgs vev [3, 69] (mass gain), or due to the bubble-bubble collision [25, 32] or due to the plasma particle−bubble collision [31]. Our study will be focused on the later one.

Let us assume that FOPT happens and the bubble expansion is indeed relativistic with $\gamma_w^{\rm terminal} \gg 1$. The simplest model where the production of heavy particles during plasma−bubble wall collision can be realized, is described by the following Lagrangian [31]:

$$\mathcal{L} = \frac{1}{2}(\partial_\mu h)^2 + i\bar{q}\partial\!\!\!/ q + i\bar{N}\partial\!\!\!/ N - M_N \bar{N} N - Y h \bar{N} q - V(h) , \tag{6.2}$$

where q is a massless particle in the symmetric phase and N is a heavy field with large vev−independent mass $M_N \gg v_{EW}$. h is the Higgs field undergoing a FOPT. With no loss of generality, we go to the basis where fermion masses are real. Before the strong phase transition starts, the abundance of heavy states N in the plasma is strongly Boltzmann suppressed and they would naively seem irrelevant for the dynamics of the transition. In an homogeneous vacuum, the transition from light to heavy state $q \to N$ is obviously forbidden by the conservation of momentum. However, in the presence of the bubble wall, the conservation of momentum along the z direction is broken (assuming a planar wall expanding in the $x-y$ plane) and a computation using WKB phases for the q and N fields demonstrates that the probability $\mathcal{P}(q \to N)$ is non-vanishing [31] and is given by

$$\mathcal{P}(q \to N) \approx \frac{Y^2 v_{EW}^2}{M_N^2} \Theta(\gamma_w T_{\rm nuc} - M_N^2 L_w) , \tag{6.3}$$

JHEP10(2022)017

with $L_w \sim 1/v_{EW}$ the width of the wall. Behind the bubble wall a large abundance of N and $\bar{N}$, n_N^{BE} is produced. Let us emphasize that this abundance is much larger than its equilibrium value.

Another possibility of the heavy particle production can be realized for the following interaction

$$\Delta\mathcal{L} \supset \frac{\lambda_{h\phi}}{2}\phi^2 h^2 + \frac{1}{2}M_\phi^2\phi^2. \tag{6.4}$$

In this case ϕ is a heavy scalar field with mass $M_\phi \gg v_{EW}$, then in the vicinity of the wall, the process $h \to \phi\phi$ has the probability [31]

$$\mathcal{P}(h \to \phi^2) \approx \left(\frac{\lambda_{h\phi} v_{EW}}{M_\phi}\right)^2 \frac{1}{24\pi^2}\Theta(\gamma_w T_{\rm nuc} - M_\phi^2 L_w^h). \tag{6.5}$$

The results in section 3.1 on the terminal velocity in the singlet extension of SM allow us to compute the maximal mass of the particles which can be produced during the electroweak FOPT in the singlet extension. Indeed saturating the step function in the above equation and assuming the $L_w \sim 1/v_{EW}$ we get approximately:

$$M^{MAX} \approx \frac{400\ \text{GeV}}{\log^{1/2}\frac{M_Z}{gT_{\rm nuc}}}\left(\frac{\Delta V - \Delta P_{\rm LO}}{(100\ \text{GeV})^4}\right)^{1/2}\left(\frac{100\text{GeV}}{T_{\rm nuc}}\right). \tag{6.6}$$

Numerical results for the maximal mass $M^{\rm MAX}$ are reported in figure 1. We can see that the maximal mass we can produce is roughly $\sim 10\,\text{TeV}$ scale.

We would like to note that our results can be easily applied for the mass gain mechanism of the heavy state production [3]. Indeed in this case the maximal mass will be $M_{\text{mass gain}} \simeq \gamma_w T$, and can be read off from the bottom right plot of the figure 1 by noting that it will scale as $M_{\text{mass gain}} \sim M_{\rm MAX}^2/v_{EW}$. Since the mass of the heavy field comes from the vev of the Higgs, it will additionally be bounded by the unitarity considerations to be below $\lesssim 2\,\text{TeV}$.

6.2 Dark Matter production

In this section we will apply the results for the velocity of the bubble expansion for DM model building.

6.2.1 Scalar DM coupled to the Higgs portal

We assume a heavy scalar ϕ coupled to the SM via the traditional Higgs portal

$$\mathcal{L}_{DM} = \frac{1}{2}(\partial_\mu\phi)^2 - \frac{M_\phi^2\phi^2}{2} - \frac{\lambda_{\phi h}}{2}h^2\phi^2\,. \tag{6.7}$$

The DM (ϕ) field is stabilized by some additional Z_2^ϕ (we use this subscript to differentiate it from Z_2 of the singlet potential). After the Higgs transition, the abundance of massive ϕ, $n_\phi^{\rm BE}$, behind the wall is given by

$$n_\phi^{\rm BE} \approx \frac{2}{\gamma_w v_w}\int \frac{d^3p}{(2\pi)^3}\frac{p_z}{p_0}\mathcal{P}(h \to \phi^2) \times f_h(p, T_{\rm nuc})\,. \tag{6.8}$$

JHEP10(2022)017

We can see that DM production during the bubble expansion is strongly dependent on the density of the Higgs field available at the nucleation temperature $f_h(p, T_{\rm nuc})$. The relevant parameter for the discussion is the ratio

$$\sqrt{\frac{d^2V}{dh^2}\Big|_{\rm fv}}\frac{1}{T} \equiv \frac{m_H^{\rm False}}{T}\,, \tag{6.9}$$

where fv denotes the position of the false vacuum and $\sqrt{d^2V/dh^2|_{\rm fv}}$ is the mass of the Higgs $m_H^{\rm False}$ in the false vacuum. As soon as this quantity becomes larger than 1, we expect exponential suppression of the Higgs abundance

$$C_{\rm eff}\frac{\zeta(3)T_{\rm nuc}^3}{\pi^2} \equiv \int \frac{d^3p}{(2\pi)^3} f_h(p, T_{\rm nuc}) \approx \begin{cases} \frac{\zeta(3)T_{\rm nuc}^3}{\pi^2} & \text{if} \quad m_H^{\rm False} < T\,, \\ \left(\frac{m_H^{\rm False}T_{\rm nuc}}{2\pi}\right)^{3/2} e^{-m_H^{\rm False}/T_{\rm nuc}} & \text{if} \quad m_H^{\rm False} > T\,. \end{cases} \tag{6.10}$$

Here we define $C_{\rm eff}$ to take into account the Boltzmann suppression. After redshifting to today, the stable produced abundance takes the form

$$\begin{aligned} \Omega_{\phi,\rm BE}^{\rm today}h^2 &= \frac{M_\phi n_\phi^{\rm BE}}{\rho_c/h^2}\frac{g_{\star S0}T_0^3}{g_{\star S}(T_{\rm reh})T_{\rm reh}^3} \approx 6.3\times 10^8\,\frac{M_\phi n_\phi^{\rm BE}}{\rm GeV}\frac{1}{g_{\star S}(T_{\rm reh})T_{\rm reh}^3}\,, \\ &\approx 5.4\times 10^5 \times \left(\frac{C_{\rm eff}\lambda_{h\phi}^2 v_{EW}}{M_\phi g_{\star S}(T_{\rm reh})}\right)\left(\frac{v_{EW}}{\rm GeV}\right)\left(\frac{T_{\rm nuc}}{T_{\rm reh}}\right)^3 \times e^{-\frac{M_\phi^2}{2\gamma_w v_{EW}T_{\rm nuc}}}\,. \end{aligned} \tag{6.11}$$

This expression has to be supplemented with the *freeze-out*(FO) contribution which is produced *before* the phase transition

$$\begin{aligned} \Omega_{\phi,\rm FO}^{\rm today}h^2 &\approx 0.1\times\left(\frac{T_{\rm nuc}}{T_{\rm reh}}\right)^3 \times \left(\frac{0.03}{\lambda_{\phi h}}\right)^2\left(\frac{M_\phi}{100\ \rm GeV}\right)^2\,, \\ \Omega_{\phi,\rm tot}^{\rm today}h^2 &= \Omega_{\phi,\rm BE}^{\rm today}h^2 + \Omega_{\phi,\rm FO}^{\rm today}h^2\,. \end{aligned} \tag{6.12}$$

Note that the FO contribution is suppressed by the factor $(T_{\rm nuc}/T_{\rm reh})^3$ due the brief stage of inflation during the phase transition. Obviously the prediction for relic density must match the experimental observations: $\Omega_{\phi,\rm tot}^{\rm today}h^2 \approx 0.1$. We can see from eqs. (6.11), (6.12) that for small values of the portal coupling $\lambda_{h\phi}$, DM production will be dominated by the freeze out mechanism while bubble expansion takes over for larger values of $\lambda_{h\phi}$.

Next we can check whether this mechanism for DM production can lead to viable phenomenology, given the results on bubble dynamics in section 5. Instead of making a scan of the parameter space, we will just focus on a few representative benchmark points.

For $m_s = 125\,\rm GeV$, $v_s = 205\,\rm GeV$, we show in figure 6 the isocontours reproducing the correct relic density for three reference values of λ_{hs} (corresponding nucleation temperatures can be found in the table 1). Firstly, $C_{\rm eff} \simeq 1$ for all three reference points. For $\lambda_{hs} = 0.424$ the upper red curve corresponds to the case when DM production is dominated by the BE (bubble expansion) and the lower curve by FO. The steepness of the upper red curve (BE) comes from the fact that we are always in the region of parameter

JHEP10(2022)017

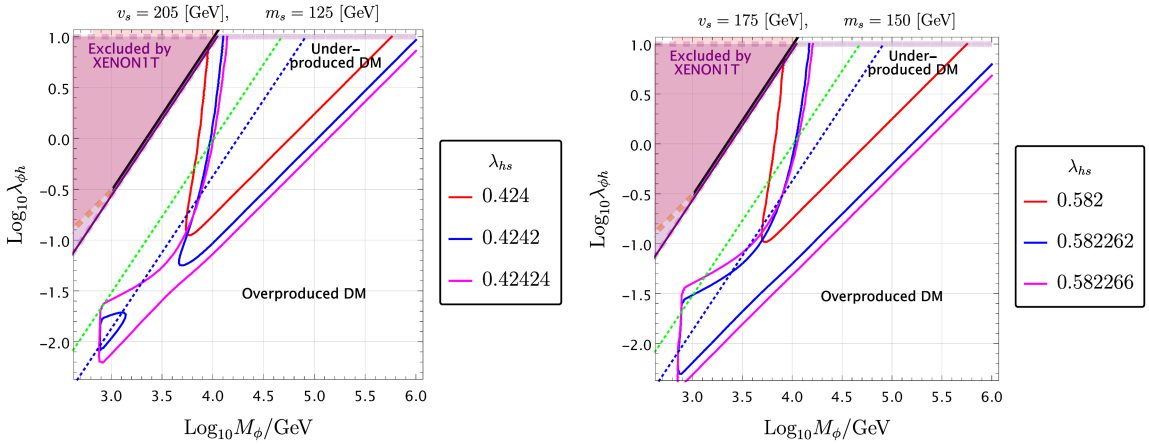

Figure 6. **Left**: dM abundance in the parameter space $\lambda_{\phi h} - M_\phi$ for different values of λ_{hs} by fixing $v_s = 205\,\mathrm{GeV}$ and $m_s = 125\,\mathrm{GeV}$ (that fixes the values of $T_{\mathrm{nuc}}, T_{\mathrm{reh}}$ and $\gamma_w^{\mathrm{terminal}}$). The solid lines represent correct DM abundance, while underproduced inside and overproduced outside. The lower part of each contour is dominated by freeze-out and the upper part via bubble expansion. The connecting vertical line (independent of the portal) comes from thermal production after the reheating of the transition. The magenta shaded region is excluded by XENON1T while the dotted green and blue lines are projected limits from XENONnT and DARWIN respectively. **Right**: same plot for $v_s = 175\,\mathrm{GeV}$ and $m_s = 150\,\mathrm{GeV}$. As expected, increasing the tuning from red to magenta increases the amplitude of the curve. The values used are extracted from table 3.

space where $\exp\left[-M_\phi^2/(2\gamma_w v_{EW} T_{\mathrm{nuc}})\right] \ll 1$, leading to a very strong sensitivity on M_ϕ mass. Physically this means that the model generically predicts large overproduction of DM in BE process unless the Boltzmann suppression $\exp\left[-M_\phi^2/(2\gamma_w v_{EW} T_{\mathrm{nuc}})\right]$ is playing a role. For the other two reference points $\lambda_{hs} = 0.4242, 0.42424$ we can see that there is an additional part of parameter space for the DM masses $M_\phi \sim 1 - 4\,\mathrm{TeV}$, which corresponds to the region without the Boltzmann suppression $\exp\left[-M_\phi^2/(2\gamma_w v_{EW} T_{\mathrm{nuc}})\right] \sim 1$. This is related to larger values of $M^{\mathrm{MAX}} \sim \sqrt{\gamma_w v_{EW} T_{\mathrm{nuc}}}$ and smaller values of the nucleation temperature, reducing the excess of the DM abundance. On the right panel of figure 6, we report similar plots for $v_s = 175\,\mathrm{GeV}$, $m_s = 150\,\mathrm{GeV}$.

Finally, before closing this section, we comment about the possibility of considering the singlet s itself, in the limit of very precise Z_2, as DM. After the phase transition $T \sim 40\,\mathrm{GeV}$, the singlet is in thermal equilibrium and we can apply straightforwardly the freeze-out expression:

$$\Omega_{s,\,\mathrm{FO}}^{\mathrm{today}} h^2 \approx 0.1 \left(\frac{0.06}{\lambda_{hs}}\right)^2 \left(\frac{M_s(v_{EW}, 0)}{100\ \mathrm{GeV}}\right)^2 . \tag{6.13}$$

From this estimate of the FO abundance for s and recalling that we considered $\lambda_{hs} \sim 0.3 - 0.6$ and $M_s(v_{EW}, 0) \sim 100\,\mathrm{GeV}$, we conclude that the abundance of s produced in this fashion, today, is underproduced by one or two orders of magnitude to fit the observed amount of DM $\Omega_{s,\,\mathrm{FO}}^{\mathrm{today}} h^2 \approx 0.1$. Even in this underproduced case, there are severe bounds from the direct detection experiments except for the resonant region, where (6.13) is over-

JHEP10(2022)017

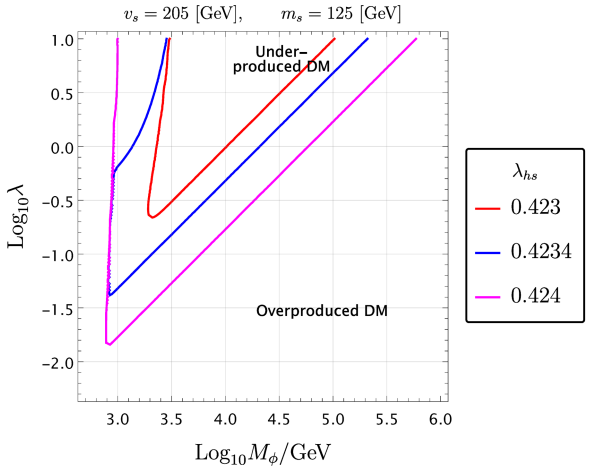

Figure 7. DM production for the singlet portal model. In this context, the Boltzmann suppression $\sim e^{-m_s/T_{\rm nuc}}$ plays a strong role and allows for bubble expansion produced DM with much higher nucleation temperature $T_{\rm nuc} \sim 15\,\mathrm{GeV}$.

estimated. However, as we will discuss in the appendix D, we will have a Z_2 explicit breaking which makes s decay much before today.

6.2.2 Singlet portal DM

In this section we mention an alternate possibility of coupling the DM (ϕ) to the singlet field s via "singlet portal"

$$\Delta\mathcal{L} \supset \frac{\lambda_{s\phi}}{2}\phi^2 s^2 + \frac{1}{2}M_\phi^2\phi^2\,, \quad \mathcal{P}(s\to\phi^2) \approx \left(\frac{\lambda_{s\phi}v_s}{M_\phi}\right)^2 \frac{1}{24\pi^2}\Theta(\gamma_w T_{\rm nuc} - M_\phi^2 L_w^s)\,, \tag{6.14}$$

where the width of the singlet wall is similar to the length of the Higgs wall L_w. Interestingly even though FOPT is from $(0, v_s) \to (v_{EW}, 0)$, the singlet scattering of the wall can lead to the production of the ϕ field. Phenomenology of DM production is very similar to the Higgs portal case discussed in the previous section, with one main difference: in the false vacuum, the mass of the singlet is not small and the factor $C_{\rm eff}$ introduced in the eq. (6.10) plays an important role. The results are shown in figure 7. For example, if we compare the curves for $\lambda_{hs} = 0.424$, $m_s = 125\,\mathrm{GeV}$, $v_s = 205\,\mathrm{GeV}$ in figure 7 and in figure 6, we can see that, for the Higgs portal DM, the isocontour has the same shape, but with the larger values of DM M_ϕ masses. As shown in eq. (6.11), this is due to the proportionality between the DM relic abundance produced during the bubble expansion with $\propto C_{\rm eff}/M_\phi$.

Singlet portal with additional field. A slight modification of this scenario is to further introduce a light scalar $\tilde{s}$. Then we can have,

$$\mathcal{L} = \mathcal{L}_{SM} - \tilde{\lambda}\tilde{s}s\phi^2 - \frac{M_\phi^2}{2}\phi^2, \tag{6.15}$$

where again ϕ is the DM and we did not write down the mass terms for simplicity of notation. We assume that $\tilde{s}$ is in the thermal bath before the PT. Then due to the field

JHEP10(2022)017

change of s in the bubble wall, the momentum conservation violating process $\tilde{s} \to \phi\phi$ can occur ($h \to \phi\phi$ may also occur if there is the $h^2\phi^2$ term.) In this model $s \to \tilde{s} + SM$ particles happen via the DM loop.

6.2.3 Fermion-mediated Dark Matter

In the previous section we noticed that the DM production during bubble expansion strongly depends on the mass of the incoming particle in the symmetric phase, due to the Boltzmann suppression factor. In case of an incoming scalar, generically this effect is relevant and crucially modifies the phenomenology, as we have seen in the section 6.2.2. In this section we construct a model where the incoming particle is a massless fermion in the symmetric phase, so that $C_{\rm eff} \equiv 1$ by definition. The model consists of a vector-like neutral fermion N which is a singlet under SM and a couple of Z_2 odd fields ϕ and χ:

$$\mathcal{L} = \mathcal{L}_{SM} + Y_* \bar{L} H N + M_N \bar{N} N + Y_{DM} \bar{N} \chi \phi \,. \tag{6.16}$$

Here, L, H are SM lepton and Higgs doublets, respectively. The production mechanism works as follows: the heavy field N is produced during the phase transition $L \to N$ and it will subsequently decay into $N \to \chi\phi, N \to LH$. The field N can be Majorana or Dirac (in the former case there will be a relation to neutrino masses and in the later it will be completely independent from neutrinos).

In this model, heavy N are produced via $L \to N$ with a probability

$$\mathcal{P}^{\rm tree}(L \to N) \approx \frac{Y_\star^2 v_{EW}^2}{M_N^2} \Theta(\gamma_w T_{\rm nuc} - M_N^2 L_w) \,. \tag{6.17}$$

As a consequence, unstable heavy N accumulate behind the wall with initial density given by

$$\begin{aligned} n_N^{\rm BE} &\approx \frac{Y_\star^2 v_{EW}^2}{M_N^2 \gamma_w v_w} \int \frac{d^3p}{(2\pi)^3} \frac{p_z}{p_0} \times f_L(p, T_{\rm nuc}) \Theta(p_z - M_N^2/v_{EW}) \,, \\ &\approx \frac{Y_\star^2 v_{EW}^2 T_{\rm nuc}^3}{2\pi^2 M_N^2} e^{-\frac{M_N^2}{2 v_{EW} T_{\rm nuc} \gamma_w}} + \mathcal{O}(1/\gamma_w) \,, \end{aligned} \tag{6.18}$$

where $v_w = \sqrt{1 - 1/\gamma_w^2}$, we expanded for large γ_w and approximated the Fermi-Dirac distribution as a Boltzmann distribution. Compared to the original proposal in ref. [2], the density of the heavy fields inside the bubble will be additionally enhanced by $\sim 16\pi^2$ factor since $1 \to 1$ transitions are more effective than $1 \to 2$. Let us assume that $M_\phi < M_\chi$ so that ϕ is the DM candidate, then DM production will happen via the following chain of processes:

$$L \underset{\text{via PT}}{\to} N \underset{\text{via decay}}{\to} \phi\chi \to \phi\phi + \text{SM} \,. \tag{6.19}$$

However, the heavy N has two channels of decay: toward the heavy dark sector ϕ, χ and back to the light L. The abundance of ϕ, χ after the transition is thus suppressed and given by

$$n_\chi \approx n_\phi \approx \frac{Y_{DM}^2 Y_\star^2}{Y_{DM}^2 + Y_\star^2} \frac{v_{EW}^2 T_{\rm nuc}^3}{2\pi^2 M_N^2} e^{-\frac{M_N^2}{2 v_{EW} T_{\rm nuc} \gamma_w}} + \mathcal{O}(1/\gamma_w) \,, \tag{6.20}$$

JHEP10(2022)017

and the final relic abundance redshifted to today thus reads

$$\Omega^{\rm today}_{\phi,\rm BE}h^2 \approx 1.5\times10^8\times\frac{Y_\star^2Y_{DM}^2}{Y_\star^2+Y_{DM}^2}\frac{2M_\phi}{M_N}\left(\frac{v_{EW}}{M_N}\right)\left(\frac{v_{EW}}{246\rm GeV}\right)\left(\frac{T_{\rm nuc}}{T_{\rm reh}}\right)^3 e^{-\frac{M_N^2}{2v_{EW}T_{\rm nuc}\gamma_w}}. \tag{6.21}$$

For the freeze-out process in the symmetric phase, we have: $\phi\phi \to LHLH$ by neglecting co-annihilation. The cross-section is highly phase space suppressed (closing a loop for a 2 to 2 annihilation gives a similar scaling): $\sigma_{\phi\phi\to(LH)^*LH} \sim \frac{M_\chi^2(Y_{\rm DM}Y_*)^2}{(16\pi^2)^2 4\pi M_N^4}$. The abundance by taking account the supercooling is

$$\Omega^{\rm today}_{\phi,\rm FO}h^2 = 10^3\left(\frac{T_{\rm nuc}}{T_{\rm reh}}\right)^3\frac{M_N^4/M_\chi^2}{(6\rm TeV)^2}\frac{10}{(Y_{\rm DM}Y_*)^4}. \tag{6.22}$$

The total DM density today will be given by the sum of eq. (6.21)–(6.22). Therefore, this scenario leads to the over-production of DM unless $M_\phi, M_\chi \lesssim 10\,\rm GeV$. However, note that these equations are valid only for the heavy DM candidates which do not go back to equilibrium after the phase transition. Otherwise, the final density will be given by eq. (6.22) only without $(T_{\rm nuc}/T_{\rm reh})^3$ and we are going back to the normal freeze-out scenario.

Let us now investigate the regime $M_\phi \simeq M_\chi$, precisely $|M_\phi - M_\chi| \lesssim M_\phi/20$, where the co-annihilation takes place. In this case we have the channel $\phi\chi \to H\bar{L}$ to decrease the abundance of ϕ as well as χ. The cross-section is $\sigma_{\phi\chi\to H\bar{L}} \sim \frac{(Y_{\rm DM}Y_*)^2}{4\pi M_N^2}$. Therefore, we have

$$\Omega^{\rm today}_{\phi,\rm FO,Co}h^2 \sim 0.1\left(\frac{T_{\rm nuc}}{T_{\rm reh}}\right)^3\times\frac{M_N^2}{(10\rm TeV)^2}\frac{1}{(Y_{\rm DM}Y_*)^2}. \tag{6.23}$$

Summing this estimate with the $\Omega^{\rm today}_{\phi,\rm BE}h^2$ in eq. (6.21) we find that it becomes possible to reproduce the observed DM abundance. However we see that bubble expansion tends to overproduce the DM and the relic abundance in BE can be reproduced if only the factor $\exp[-M_N^2/(2v_{EW}T_{\rm nuc}\gamma_w)]$ starts playing a role in suppressing DM relic density (left boundary of figure 8 is almost vertical).

6.3 Baryogenesis mechanism

Now we remind the scenario of Baryogenesis with relativistic bubble walls that was proposed in [1]. As a prototype, we worked with the following model, reminiscent of the toy model of eq. (6.2), (omitting the kinetic terms)

$$\begin{aligned}\mathcal{L} = \mathcal{L}_{SM} + m_\eta^2|\eta|^2 + \sum_{I=1,2} M_I\bar{B}_IB_I \\ + \left(\sum_{I=1,2} Y_I(\bar{B}_IH)P_LQ + y_I\eta^*\bar{B}_IP_R\chi + \kappa\eta^c du + \frac{1}{2}m_\chi\bar{\chi^c}\chi + h.c.\right).\end{aligned} \tag{6.24}$$

Thus, additionally to the SM and the singlet sector, the model contains a Majorana field χ and two vector-like B quarks with the masses $M_{1,2} \sim m_\chi$. η is a scalar field in the fundamental representation of QCD and with electric charge $Q(\eta) = 1/3$. We defined Q, u, d as the SM quark doublet and singlets respectively, and ignored the flavour indices. H is the SM Higgs.

JHEP10(2022)017

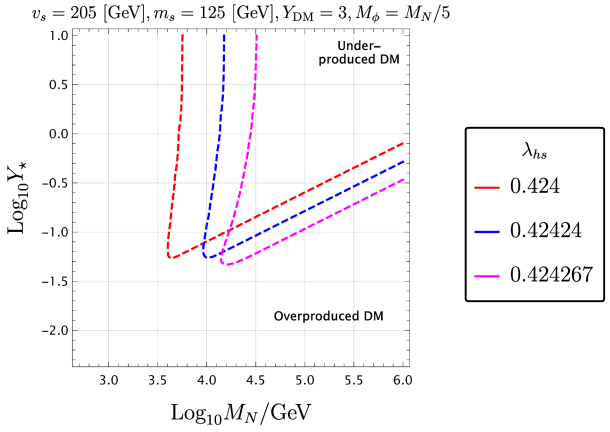

Figure 8. DM production in the fermionic portal model. We fix $M_{\rm DM} = M_N/5$, and $Y_{\rm DM} = 3$. Only the co-annihilation regime where $|M_\phi - M_\chi| \lesssim M_\phi/20$ appears to be viable and shown by dashed lines.

We first proved that the production mechanism, when computed up to one loop-level, indeed transforms a CP-violating phase into a chiral asymmetry in the abundances produced, in a fashion very similar to usual leptogenesis decay. Let us now sketch the mechanism in itself. First, $b-$quarks collide with the relativistic wall and produce B_I, B_I^c via the mechanism explained above. Thus inside the bubble we have

$$n_{B_I} - n_{B_I^c} = -\left(\frac{Y_I v_{EW}}{M_I}\right)^2 \epsilon_I n_b^{\rm inc}\,, \qquad n_b - n_{b^c} = \sum_I \left(\frac{Y_I v_{EW}}{M_I}\right)^2 \epsilon_I n_b^{\rm inc}\,, \tag{6.25}$$

where $n_b^{\rm inc}$ is the number density of the bottom-type quark colliding with the wall from outside, n_b and n_B are the abundances inside of the bubble and ϵ is a loop suppressed coefficient which parametrizes the CP violating phase and the resonance between one-loop and tree-level diagrams. After the passage through the wall, the following asymmetric abundances are then generated

$$\sum_I \left(n_{B_I} - n_{B_I^c}\right) = -(n_b - n_{b^c})\,. \tag{6.26}$$

From this expression we can read an apparent asymmetry in the bottom quark abundances. However, if the heavy B freshly produced were to decay back into b, the asymmetry would be washed out. This is however not the case if they decay in a dark sector containing χ, η, where the asymmetry is enhanced by the presence of a Majorana mass for χ. The final unsuppressed produced asymmetry is given by

$$\begin{aligned}\frac{\Delta n_{\rm Baryon}}{s} \approx \frac{135\zeta(3)}{8\pi^4} \sum_{I,J} \left(\frac{Y_I \langle H\rangle}{M_I}\right)^2 \frac{|y_I|^2}{|y_I|^2 + |Y_I|^2} \times \frac{g_b}{g_\star}\left(\frac{T_{\rm nuc}}{T_{reh}}\right)^3 \\ \times\ {\rm Im}(Y_I Y_J^* y_I^* y_J) \left(-\frac{2{\rm Im}[f_B^{IJ}]}{|Y_I|^2} + \frac{4{\rm Im}[f_B^{IJ}]|_{m_{\chi,\eta}\to 0}}{|y_I|^2}\right)\,,\end{aligned} \tag{6.27}$$

where s is the entropy at the moment of the production, g_b is number of degrees of freedom of the bottom and $g_\star$ the number of relativistic degrees of freedom. The loop functions

JHEP10(2022)017

f_B^{IJ} have been computed in [1] and are controlled by the CP violating sector. Absence of strong wash-out conditions

$$M_{B,\chi,\eta} \gtrsim 30 T_{\rm reh} \sim 10^3 \text{ GeV}\,, \qquad \text{(suppressed wash-out)} \tag{6.28}$$

as well as experimental signatures (direct production in colliders, flavor violation, neutron oscillations) pushed the heavy particles to be

$$M_{B,\chi,\eta} \gtrsim 2 \times 10^3 \text{ GeV}\,. \tag{6.29}$$

In the context of singlet extension with Z_2 that we studied, this opens up the range

$$M_{B,\chi,\eta} \in [2, 10] \text{ TeV}\,, \tag{6.30}$$

where the Baryogenesis mechanism proposed above is operative.

6.4 Impact of the heavy sector on the phase transition

The models we are considering by construction have new heavy fields coupled to the Higgs boson. These will lead to the finite corrections to the scalar parameters of the form (assuming a Yukawa type connection $yBHb$)

$$\delta m_h^2 \sim \frac{-8 g_N M_N^2 y^2}{64\pi^2}\left(\log\frac{M_N^2}{v_{EW}^2} - \frac{3}{2}\right), \qquad \delta\lambda \sim 4 g_N \frac{y^4}{64\pi^2}\left(\log\frac{M_N^2}{v_{EW}^2} - \frac{3}{2}\right), \tag{6.31}$$

where g_N is the number of heavy degrees of freedom and M_N is the typical mass of the heavy sector. One can wonder how these corrections can effect the tuning of the Higgs potential. However note that in our model the Higgs mass hierarchy problem is not addressed and generically we expect the size of m_h^2 to be of the order of the cut off scale ($M_{\rm pl}$ in SM). So the corrections in eq. (6.31) do not make the tuning worse.

In case the Higgs hierarchy problem is solved at the scale of the heavy fields in eq. (6.7), (6.24) the tuning in the Higgs potential will be roughly,

$$\text{tuning} \sim \frac{m_h^2}{\Delta_{\text{Heavy physics}} m_h^2} \sim \frac{8\pi^2 m_h^2}{y^2 M_N^2}. \tag{6.32}$$

We can combine this estimate with a tuning for low nucleation temperatures (see discussion in section 5.1) which are necessary for the heavy field production and the tuning estimate becomes:

$$\text{tuning} \sim \frac{T_{\rm nuc}^2}{\Delta_{\text{Heavy physics}} m_h^2} \sim \frac{8\pi^2 T_{\rm nuc}^2}{y^2 M_N^2}. \tag{6.33}$$

Using the estimates of the maximal values of γ_w and the maximal mass of heavy particles which can be produced during the bubble-plasma collisions (see eq. (3.18) and eq. (6.3)) we get the following estimate for the maximal tuning in the model

$$\text{tuning}^{MAX} \sim \left(\frac{T_{\rm nuc}}{20\text{GeV}}\right)^4, \tag{6.34}$$

where we remind the reader that this estimate is valid only if the Higgs hierarchy problem is solved at the heavy fields scale.

JHEP10(2022)017

7 Gravitational waves emitted

It is well known that strong gravitational waves background will be emitted, with peak frequency around the mHz if the EWPT happens to be strongly first order. This is the optimal range of sensitivity of the forthcoming LISA detector [88, 89] and also GW detectors such as eLISA [90], LIGO [91, 92], BBO [93, 94], DECIGO [95–97], ET [98–100], AION [101], AEDGE [102].

The signal produced at the moment of the transition can be separated into different contributions: the *bubble collision* [103] contribution, the *plasma sound waves* [89] and finally the *turbulence*. Only the two first sources of GW are well understood. Another nice feature of those two sources is that they are expected to dominate in different physical situations; the bubble collision would dominate in case of runaway wall and the sound waves if the wall reaches a terminal velocity. We have already mentioned that the EWPT, if first order, will always happen in the regime of terminal velocity, because of the large number of strongly coupled vector bosons.[7] For GW produced by plasma sound wave, the peak frequency and amplitude are given by

$$\begin{aligned}\Omega^{\rm peak}_{\rm plasma}h^2 &\approx 0.7\times 10^{-5}\left(\frac{100}{g_\star}\right)^{1/3}\left(\frac{\kappa_{sw}\alpha}{1+\alpha}\right)^2 (H_{\rm reh}R_\star),\\ f_{\rm peak} &\approx 2.6\times 10^{-5}\left(\frac{1}{H_{\rm reh}R_\star}\right)\left(\frac{z_p}{10}\right)\left(\frac{T_{\rm reh}}{100\ {\rm GeV}}\right)\left(\frac{g_\star}{100}\right)^{1/6}\ {\rm Hz}\end{aligned} \tag{7.1}$$

with $z_p \sim 10$, κ_{sw} is the efficiency factor for the production of sound waves in the plasma [104],

$$\kappa_{sw} \approx \frac{\alpha}{0.73+0.083\sqrt{\alpha}+\alpha}, \tag{7.2}$$

α and $R_\star$ have been defined in eqs. (3.6) and (5.2) respectively, $R_\star \sim \mathcal{O}(10^{-1}-10^{-4})H^{-1}$ is the approximate size of the bubble at collision and all quantities $(T, H, g_\star)$ have to be evaluated at *reheating*.

As we have seen in sections 6.3–6.2, for the baryogenesis and DM production we need relativistic walls with relatively low nucleation temperature $\lesssim 10\,$GeV. In this context, $\alpha \gg 1$ and $\kappa_{sw} \to 1$. The peak frequency and the signal amplitude are only function of the size of the bubbles at collision, which are reported in table 2 and 3. We can observe that in this range β/H spans the value between $[50, 10^4]$, with a preference for lower values. Going back to eq. (7.1), emitted amplitude and frequencies will be of the order

$$\Omega^{\rm peak}_{\rm plasma}h^2 \in [5\times 10^{-7}, 2\times 10^{-9}], \qquad f_{\rm peak} \in [10^{-4}, 0.03]\quad {\rm Hz} \tag{7.3}$$

where we set $z_p = 10, g_\star = 100$. This range of frequencies and amplitude are largely in the expected sensitivity of the coming observer LISA [89, 90], as expected for this class of models [36]. We thus conclude that strong GW signal in the LISA with spectrum controlled by the plasma sound waves is a generic prediction of Baryogenesis with relativistic bubble

[7] A possible exception would be the case of extreme cooling, as hinted in [72] where even the pressure from gauge bosons cannot stop the acceleration of the wall. However, in our study, we do not find such a situation.

JHEP10(2022)017

walls. This is in sharp opposition with the general expectation that usual EWBG demands slow walls, and thus suppressed signals.

As a final comment, it should however be noticed that the current simulations do not directly provide a solutions for the regime of large α, and we only have an extrapolation of the numerical result. Thus, the conclusion above should be taken with a grain of salt.

8 Conclusion

In this study we have presented the first explicit realization of the baryogenesis and DM production during electroweak phase transition for ultra-relativistic bubble expansion. The work is based on the proposals in [1–3, 31] where new heavy particles are produced in plasma−bubble wall collisions. We have shown that the model with SM extended by a real singlet with a Z_2 symmetry can indeed lead to ultra-relativistic bubbles, where the Lorentz factor γ_w can reach the values $\sim 10^{5-6}$. Such fast bubbles can appear if the symmetry breaking occurs in two steps: first discrete Z_2 is spontaneously broken and in the second step electroweak symmetry breaking is accompanied by Z_2 restoration $(0,0) \xrightarrow{SOPT} (0,v_s) \xrightarrow{FOPT} (v_{EW},0)$. We find that there exists a region of parameter space where the nucleation temperature can become as low as $1-2\,\text{GeV}$ and the collision of the bubble wall with the plasma particles can lead to the non-thermal heavy particle production with the masses up to $\sim 10\,\text{TeV}$. Interestingly we find that the mechanism is most efficient for relatively low masses of the singlet field $M_s(v_{EW},0) \sim 70-100$ GeV, close to the region excluded by the Higgs invisible decays. Subsequently, this region of parameter space will be probed by HL-LHC ([75, 105]) in the singlet production mediated by off-shell Higgs boson. By noting the slight Z_2 breaking, s, if produced, can decay into $b\bar{b}$ in collider experiments. Depending on the size of the breaking displaced vertices of $b\bar{b}$ may be probed. We find the typical bubble radius parameter of the order of $R_\star \sim (10^{-4}-1)H^{-1}$ so that stochastic gravitational background signal becomes observable at GW experiments like LISA [89, 90].

The model necessarily requires tuning $\propto (T_{\text{nuc}}/m_h)^2$ which numerically turns out to be of the order of $10^{-4}-10^{-2}$ (using Giudice-Barbieri measure) for successful baryogenesis and DM production mechanism. In spite of this we believe it can provide a useful guidance for more appealing models where these hierarchies can appear naturally.

Acknowledgments

AA and SC were supported by the MIUR contract 2017L5W2PT. WY was supported by JSPS KAKENHI Grant Nos.20H05851, 21K20364, 22K14029, and 22H01215. MV thanks the DESY institute for hospitality during the writing of this manuscript as well as Alberto Mariotti and Simone Blasi for fruitful discussions in the late stages of the completion of the paper.

JHEP10(2022)017

A The bounce in two dimensions

In this paper we studied numerically the phase transition from the minimum $(0, v_s)$ (or in the vicinity of it) to $(v_{EW}, 0)$. The bounce computation can be done using existing codes for example `FindBounce` or `CosmoTransition`. However we have found that in the regime of long supercooling where the potential around the false vacuum is very flat and, the existing codes are often not stable and lead to numerical errors. Thus we have developed our own code (more stable for the flat potentials), following the procedure described in [106], while cross-checking the available values with `FindBounce`.

A.1 Computation of the bounce profile

In this appendix, we briefly review the standard computation of the bounce action with only one field before going to describe the algorithm we used for the same computation but for the case of two fields PT. In order to compute the vacuum tunneling probability from the false vacuum to the true one in d dimensions, we need to minimize the Euclidean action given by

$$S_E = \int d^d x \left[\frac{1}{2} (\partial_\mu \phi)^2 + V[\phi] \right]. \tag{A.1}$$

It is known that the field configurations leading to the minimal action are the ones that exhibit an $O(d)$ spherical symmetry, then the so-called bounce solution is the solution of the following Cauchy problem

$$\frac{d^2\phi}{dr^2} + \frac{d-1}{r}\frac{d\phi}{dr} = \frac{dV[\phi]}{d\phi}, \qquad \lim_{r\to\infty} \phi(r) = 0, \qquad \left.\frac{d\phi}{dr}\right|_{r=0} = 0, \tag{A.2}$$

where we have chosen the false minimum to be at $\phi = 0$. If we interpret the parameter r as a time and ϕ as a position, this problem becomes formally equivalent to the evolution of a mechanical ball in a potential $-V[\phi]$ undergoing a friction $\frac{d-1}{r}\frac{d\phi}{dr}$, released with vanishing velocity and stopping its evolution for $r \to \infty$ at $\phi = 0$. It is well known that this problem can be solved by applying numerically an overshoot/undershoot method on the position of the released point. Releasing the ball too close to the true vacuum would induce an overshoot configuration (the ball would continue after crossing $\phi = 0$), we would thus shift the release point toward the false vacuum, while releasing it too close to it would end up in an undershoot configuration (the ball would never reach $\phi = 0$ and starts oscillate around the minimum of $-V[\phi]$) and we correct it by shifting the release point farther from the false vacuum. Iterating between those two situations, we are able to find the correct release point and obtain the *bounce solution*.

It is well known that the case of a PT triggered by temperature fluctuation at temperature T is formally equivalent to imposing a periodicity T^{-1} in the imaginary time t_E, which imposes the following constraint on the field

$$\phi[t_E, \vec{x}] = \phi[t_E + T^{-1}, \vec{x}] \tag{A.3}$$

and the computation of thermally induced phase transition thus amounts to take $d = 3$ in the above equations.

JHEP10(2022)017

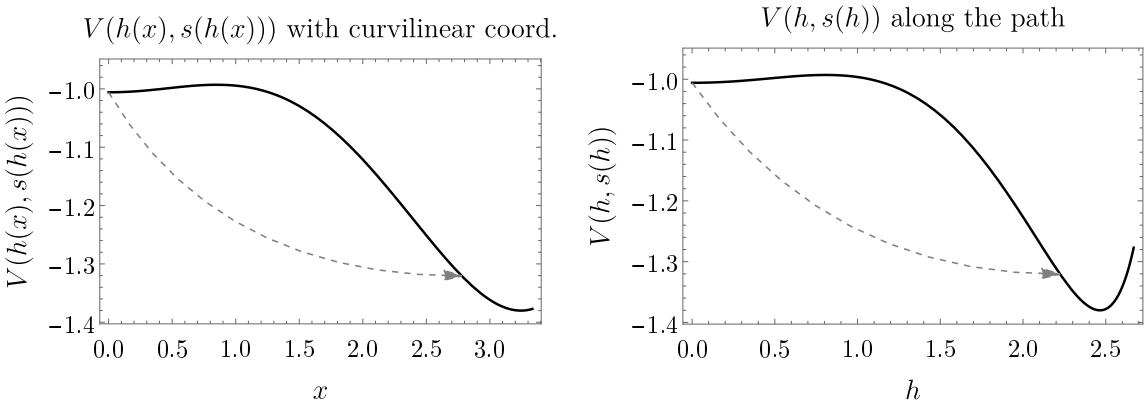

Figure 9. On the left, the potential, along the path, experienced by the field x and the corresponding escape point $x_\star$. On the right the potential, along the path, projected on the h direction.

A.2 Bounce action in two dimensions and path deformation

The problem complexifies when the transition involves many fields. Here there is no straightforward intuition for the path followed by the fields in field space during the tunneling. One can think that a straight line, connecting the two minima, could be a reasonable guess, but it turns out that it cannot be considered as a good approximation of the euclidean action.[8] Here we thus describe the algorithm [106] to find the right path in field space. In a multi-field case, the eq. (A.2) becomes

$$\frac{d^2\vec{\phi}}{dr^2} + \frac{d-1}{r}\frac{d\vec{\phi}}{dr} = \vec{\nabla}V[\vec{\phi}], \qquad \lim_{r\to\infty}\vec{\phi}(r) = 0, \qquad \left.\frac{d\vec{\phi}}{dr}\right|_{r=0} = 0. \tag{A.4}$$

Since in this case an overshoot/undershoot procedure cannot be easily applied, the idea is to reduce the problem to one dimensional tunneling. In order to do so we start guessing the path, $\vec{\phi}_g(x)$, where x is now to be understood as the parameter that measure the distance along the path, i.e. the so-called curvilinear abscissa. For the present case, if we parametrize the path in the field space as $(h(t), s(t)) = (t, f(t)) \equiv (h, s(h))$ it is defined as

$$x(h) = \int_{h_{fm}}^{h} \sqrt{1 + \left(\frac{ds(h')}{dh'}\right)^2}\, dh', \tag{A.5}$$

where h_{fm} is the value of the Higgs field in the false minimum. With this choice of field coordinate to parametrize the path, the condition $\left|\frac{d\vec{\phi}(x)}{dx}\right|^2 = 1$ is satisfied, and the Euclidean equation of motion in eq. (A.4) can be rewritten along the parallel and the perpendicular

[8] Let us emphasize that in the region of the parameter space we studied, the straight line between the false and the true vacuum gives an Euclidean action which is often wrong by *orders of magnitudes*, as the path is often very far from the straight line, as a consequence, we cannot dispense from the effort of studying the exact 2D path in field space.

JHEP10(2022)017

direction

$$\frac{d^2x}{dr^2} + \frac{d-1}{r}\frac{dx}{dr} = \partial_x V[\vec{\phi}_g(x)],$$
$$\frac{d^2\vec{\phi}_g(x)}{dx^2}\left(\frac{dx}{dr}\right)^2 = \vec{\nabla}_\perp V[\vec{\phi}_g(x)]. \tag{A.6}$$

Here, we have been able to separate the dynamics along the parallel and perpendicular direction in such a way the first equation defines a new undershoot/overshoot problem, that we solve to obtain the value of the *escape point*, $\vec{\phi}_0(x_\star)$, and the Euclidean action corresponding to the potential along the path considered $\vec{\phi}_g$, as in figure 9. On the other hand, the second equation can be seen as a condition that the bounce solution has to satisfy and can be thought as a force field acting on the path, defined as following

$$\vec{N} \equiv \frac{d^2\vec{\phi}_g(x)}{dx^2}\left(\frac{dx}{dr}\right)^2 - \vec{\nabla}_\perp V[\vec{\phi}_g(x)]. \tag{A.7}$$

The right path will be the one where $\vec{N}$ is vanishing. The algorithm proceeds iteratively: first we guess a path, the straight line connecting the two minima, then we find the bounce solution along this path, we compute the normal force and deform the guessed path according to it. In practice, to define the path at the step n, $\vec{\phi}_n$, we need to solve for the bounce profile for the path at $\vec{\phi}_{n-1}$, extract the escape point $x_{\star,n-1}$, that is $(h(x_{\star,n-1}), s(x_{\star,n-1}))$ in field space, we then discretize the path in the interval $x \in [0, x_{\star,n-1}]$, creating a series $(\vec{\phi}_{n-1})_j$, for $j = 1, \ldots, N$ and a series of values for the normal force $(\vec{N}_{n-1})_j$. We then shift each point of the discretized path by

$$(\vec{\phi}_n)_j = (\vec{\phi}_{n-1})_j + \rho(\vec{N}_{n-1})_j \qquad j = 1, \ldots, N. \tag{A.8}$$

In the end, we fit a path $\vec{\phi}_n$ along the shifted points from $(\vec{\phi}_{n-1})_j$. The procedure of deformation of the path will produce a series of paths $\vec{\phi}_i[x]$, over which we compute the Euclidean action according to eq. (A.1) at each step of the deformation, like in figure 10. The algorithm stops when the difference in the bounce action, S_3, between two successive iterations is below some imposed precision. At a definite temperature T, we start by identifying the two minima, the false and the true ones

$$(\langle h \rangle, \langle s \rangle)_{\rm fm} = (v(T), v_s(T)) \to (v_{EW}, 0), \tag{A.9}$$

and will keep the false minimum fixed during the whole procedure of deformation. Generally, especially when we have a sizable amount of supercooling, the escape point is just behind the barrier, so the escape point $(v_\star(T_n), v_{s,\star}(T_n))$ will be different from the, zero-temperature, EWSB vacuum, but when the tunneling happens the system will classically roll down towards the global minimum, as we can see from figure 10. We do not track the evolution of the fields profile after the tunneling.

B Supplemental numerical results

In this appendix, we present all our supplemental numerical results. First, tough we focused mostly on a more weakly coupled part of the parameter space, we would like to compare

JHEP10(2022)017

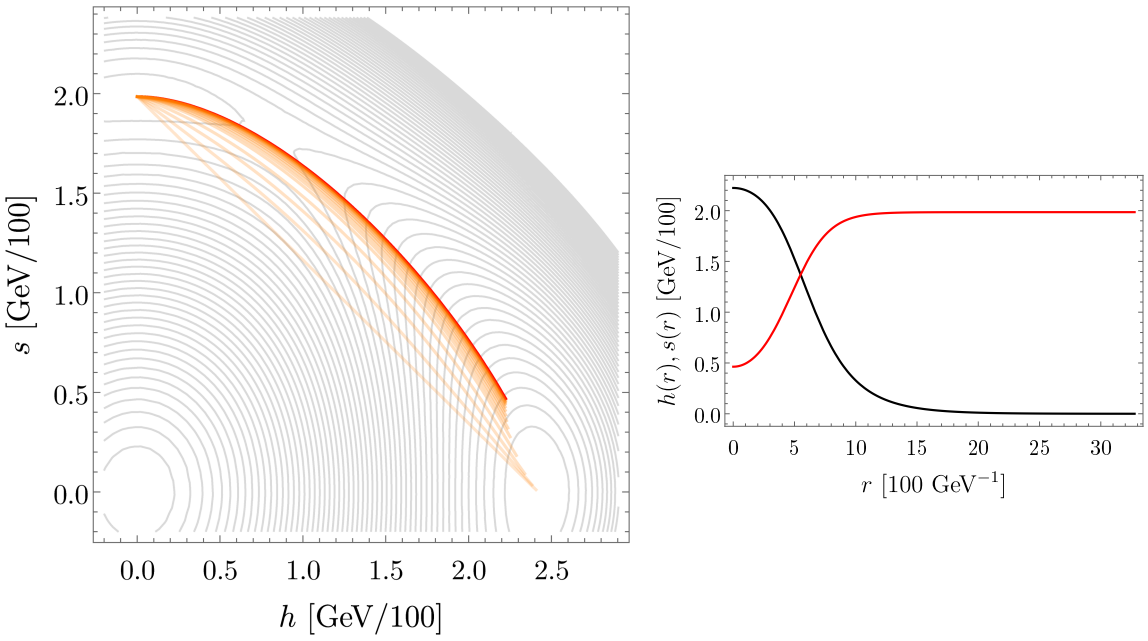

Figure 10. **Left**: iterative procedure for the correct path, starting from the straight line connecting the two minima and then modified according to the field $\vec{N}$. **Right**: bounce profile of the fields (black for $h(r)$ and red for $s(r)$) on the correct path.

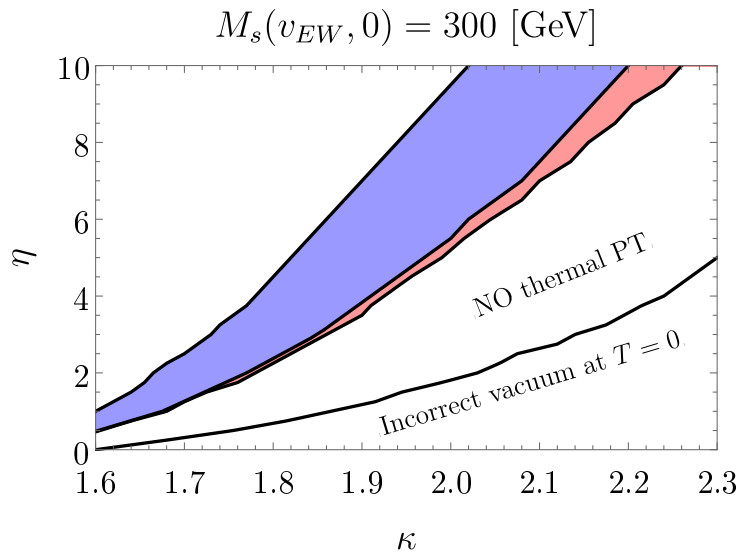

Figure 11. Here is presented the same results found in figure 6 of ref. [49]. It has to be noted that these results are obtained with only the thermal potential and without Daisy resummation, i.e. without thermal masses. The relation with our parameters is $(\lambda_s,\ \lambda_{hs}) = (\eta,\ 2\kappa)$ and $M_s(v_{EW}, 0) = 300\,\text{GeV}$.

JHEP10(2022)017

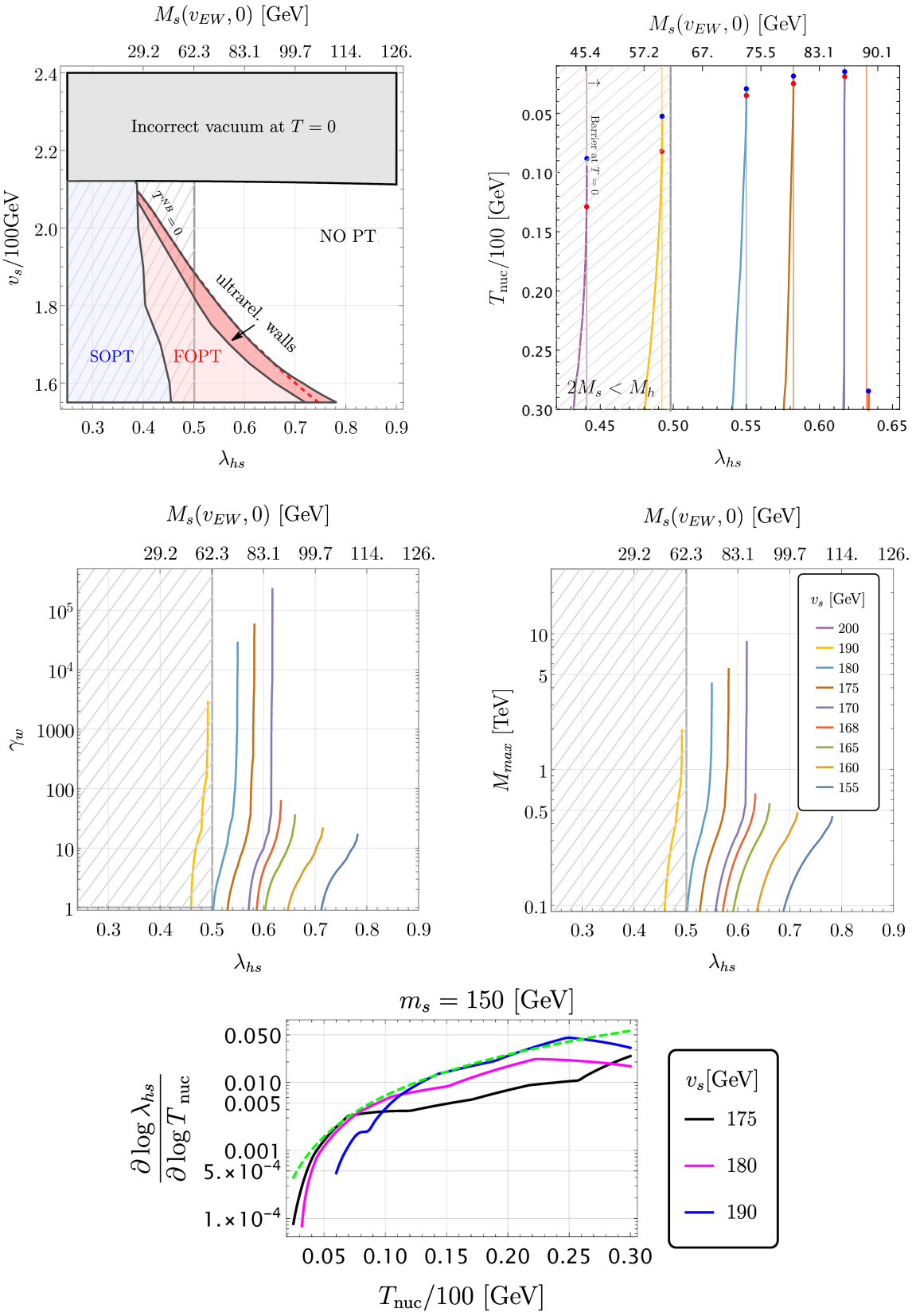

Figure 12. Similar plots than in figure 1 and figure 3 for the value of $m_s = 150\,\text{GeV}$.

JHEP10(2022)017

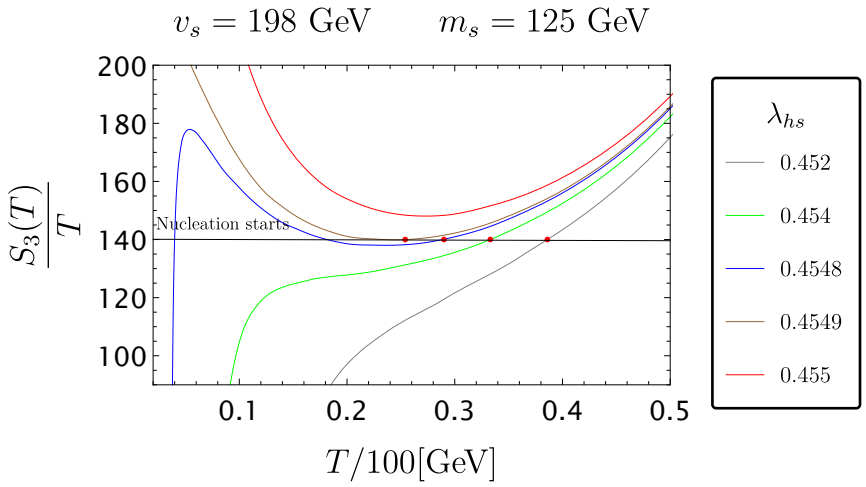

Figure 13. On this plot we show the regime of transition. We observe that several points display a disappearance of the barrier which is typical of the regime of no barrier at $T = 0$. However, the nucleation temperature is controlled by the first minimum of S_3/T, which is typical of the regime with a barrier at $T = 0$.

$m_s = 150\,\text{GeV}, \quad v_s = 175\,\text{GeV}$							
λ_{hs}	$\frac{T_{\text{reh}}}{100\text{GeV}}$	$\frac{T_{\text{nuc}}}{100\text{GeV}}$	$\frac{T_{\text{per}}}{100\text{GeV}}$	γ_w	$\frac{\tilde{\beta}}{H} = \frac{(8\pi)^{1/3}}{R_\star H}$	$m_H^{\text{False}}/\text{GeV}$	FM_0
0.53	0.616	0.608	0.592	–	580	17.4	No
0.54	0.581	0.570	0.552	3	420	17.8	No
0.56	0.492	0.470	0.444	9	228	17.7	No
0.58	0.329	0.141	0.130	348	160	4.7	No
0.582	0.327	0.051	0.0508	$5.3 \cdot 10^3$	$9.5 \cdot 10^3$	0.4	No
0.582262	0.327	0.025	0.0236	$3.7 \cdot 10^4$	194	8.2	Yes
0.582264	0.327	0.024	0.0219	$4.3 \cdot 10^4$	130	8.3	Yes
0.582266	0.327	0.021	0.017	$5.7 \cdot 10^4$	24	8.5	Yes

Table 3. Same as tables 1 and 2, but with $m_s = 150$ GeV and $v_s = 175\,\text{GeV}$.

our findings with the ones in the ref. [49] and argue that we observed only small changes, due to the inclusion of loop-corrections and Daisy resummation. On figure 11 we make a reproduction of the scan of the figure6 of [49] using our potential and emphasize the close similarities. The relations between the parameters κ, η and the couplings in the eq. (2.1) is as follows

$$\kappa_{[49]} = \frac{\lambda_{hs}}{2}, \quad \eta_{[49]} = \lambda_s. \tag{B.1}$$

In the main text, we studied specifically the case where the parameter $m_s = 125\,\text{GeV}$, we observed that for this value, the region of deep supercooling displayed small masses of the singlet in the real vacuum, being on the verge of detection due to $h \to ss$ at $M_s \lesssim 62\,\text{GeV}$. We also concluded in section 5 that this region was closing around $M_s \approx 75\,\text{GeV}$. We could wonder if this conclusion would change if we modify the value of the parameter m_s, and if

JHEP10(2022)017

so in which direction. On figure 12 we show similar plots than in figure 1 and 3 for the case of $m_s = 150\,\text{GeV}$. Thus, increase the value of m_s pushes the deep supercooling region to $M_s \approx 90\,\text{GeV}$, at the price of increasing the portal coupling λ_{hs}. However, we can observe on the last plot of figure 12 that the typical tuning remains roughly the same and that we can still trust our naive $(T_{\text{nuc}}/m_h)^2$ for an order-of-magnitude estimate of the tuning.

On the other hand, we also observed that decreasing the parameter m_s to $\approx 100\,\text{GeV}$ was pushing all the deep supercooling region inside $M_s \lesssim 62\,\text{GeV}$, which is thus strongly disfavored by colliders. We hope that this trend can be extrapolated to larger values of m_s, until we hit perturbativity bounds for λ_{hs}.

We could also wonder what happens at the *upper* boundary of the deep supercooling region, as we have observed on figure 1 a sharp decrease in the supercooling allowed around $v_s \lesssim 200\,\text{GeV}$ (for $m_s = 125\,\text{GeV}$). This transition regime can be understood if we plot the explicit S_3/T functions on figure 13. Comparing the plot in figure 13 with the one in figure 4, we see that as we decrease v_s, the full pattern of S_3/T is shifted toward smaller values. At some critical point around $v_s \approx 200\,\text{GeV}$, the nucleation becomes controlled by the first minimum in the function S_3/T and not by the disappearance of the barrier. This largely suppresses the possibility for large supercooling.

Finally, in table 3, we provide the value of the velocity, reheating and nucleation temperature for $m_s = 150\,\text{GeV}$ and $v_s = 175\,\text{GeV}$ that was used in figure 6.

C The coefficient of NLO pressure

In this appendix we will review the calculation of the friction coefficient for the NLO pressure for EW phase transition. We will follow closely the discussion in [72] and report the quantity

$$\left[\sum_{abc} \nu_a g_a \beta_c C_{abc}\right] \tag{C.1}$$

where $\nu_a = 1(3/4)$ for a a boson (fermion), $\beta_c \equiv \frac{M_c}{M_Z}$and C_{abc} stands for the couplings appearing in the vertex. Normalization of the C_{abc} coefficient is the following: for a chiral fermion coupled to the vector field the amplitude for the process $\psi \to \psi A_{soft}$ is equal to

$$g_\psi \bar{\psi}_L A_\mu \psi_L \Rightarrow \quad C_{\psi\psi A} = \frac{g_\psi^2}{4\pi\alpha_{em}}. \tag{C.2}$$

The relation eq. (C.2) is written only for one polarization of the vector field. Similarly for the scalar field

$$i g_\phi (\phi^* \partial_\mu \phi - \partial_\mu \phi^* \phi) A^\mu \Rightarrow \quad C_{\phi\phi A} = \frac{g_\psi^2}{4\pi\alpha_{em}}, \tag{C.3}$$

and the vector fields

$$g_{V^1V^2A^3}\left(V^1_{\mu\nu} V^2_\mu A_\nu + V^2_{\mu\nu} A_\mu V^1_\nu + A_{\mu\nu} V^1_\mu V^2_\nu\right) \Rightarrow C_{V_1V_2A} = \frac{g^2_{V^1V^2A}}{4\pi\alpha_{em}}, \tag{C.4}$$

where in all of these formulas C_{abc} coefficients are reported only for one polarization of the vector fields both in the initial and the final states. Summing all of these contributions

JHEP10(2022)017

Process	$\sum g_a C_{abc}$	β	ν	Result
$\psi \to W^{\pm}\psi$	$\frac{24}{s_w^2}$	c_w	$\frac{3}{4}$	$\frac{18c_w}{s_w^2}$
$\psi \to Z\psi$	$\frac{4(3-6s_w^2+8s_w^4)}{s_w^2 c_w^2}$	1	$\frac{3}{4}$	$\frac{3(3-6s_w^2+8s_w^4)}{s_w^2 c_w^2}$
$\mathcal{H} \to W\mathcal{H}$	$\frac{2}{s_w^2}$	c_w	1	$\frac{2c_w}{s_w^2}$
$\mathcal{H} \to Z\mathcal{H}$	$\frac{1-2s_w^2c_w^2+c_w^4+s_w^4}{2s_w^2c_w^2}$	1	1	$\frac{1-2s_w^2c_w^2+c_w^4+s_w^4}{2s_w^2c_w^2}$
$A \to W_{soft}W$ & $W \to W_{soft}A$	8	c_w	1	$8c_w$
$Z \to W_{soft}W$ & $W \to W_{soft}Z$	$\frac{8c_w^2}{s_w^2}$	c_w	1	$\frac{8c_w^3}{s_w^2}$
$W \to Z_{soft}W$	$\frac{4c_w^2}{s_w^2}$	1	1	$\frac{4c_w^2}{s_w^2}$
Total:				$2\left(\frac{7+14c_w}{s_w^2} - \frac{7-15s_w^2}{c_w^2}\right) \simeq 157$

Table 4. Different contributions to the sum in eq. (3.15).

and taking care of the multiplicities of the initial and final states we find

$$\left[\sum_{abc} \nu_a g_a \beta_c C_{abc}\right] = 2\left(\frac{7+14c_w}{s_w^2} - \frac{7-15s_w^2}{c_w^2}\right) \simeq 157. \tag{C.5}$$

For the interested reader we refer various individual contributions in the table 4. If in the false vacuum the Higgs doublet $\mathcal{H}$ is too heavy its contribution must be subtracted and the sum in eq. (C.5) reduces to

$$\left[\sum_{abc} \nu_a g_a \beta_c C_{abc}\right]_{\text{No Higgs}} \simeq 145. \tag{C.6}$$

At last we would like to emphasize that these results include only the transverse polarizations of the vector fields. NLO effects of the longitudinal polarizations are not fully established and we omit them here, however these cannot qualitatively modify the results.

D Domain wall collapse

Our main discussion was focused on the two step phase transition $(0,0) \to (0,v_s) \to (v_h,0)$ where the first phase transition is Z_2 breaking. Obviously during such a phase transition domain walls will be formed which can drastically modify the cosmology of the system. We can avoid the stable domain walls if we assume some small Z_2 breaking, however in this case the question rises about the timescale for the stability of the domain walls. This is particularly important since recently it was shown [107] that for singlet extension of the SM the domain walls (if still present) will become seeds of the secondary phase transition $(0,v_s) \to (v_h,0)$ and will dominate the phase transition. We will follow closely the discussion in the section 4.2 using only the tree level potential and the thermal corrections

JHEP10(2022)017

to the masses. Then the Z_2 breaking phase transition will occur at the temperatures

$$T_{Z_2} \simeq v_s \left(\frac{12}{3 + 4\lambda_{hs} \frac{v_s^2}{m_s^2}} \right)^{1/2} \simeq 200 - 300 \ \ \text{GeV}, \tag{D.1}$$

which is a temperature of the domain wall formation. The domain wall mediated transition will happen at the temperature T_w which is found to be order one different from T_{Z_2}. The exact mechanism of the transition depends on the values of the couplings and can proceed either with the classical rolling or 2D bounces localized on the domain wall. The temperature when the classical rolling can start is reported in ref. [107] and is equal to

$$T_w^{\text{rolling}} \simeq T_{Z_2} \left[\frac{4m_h^2 + m_s^2 \left(1 - \sqrt{1 + \frac{8v_s^2 \lambda_{hs}}{m_s^2}} \right)}{8\Pi_h(T_{Z_2}) + m_s^2 \left(1 - \sqrt{1 + \frac{8v_s^2 \lambda_{hs}}{m_s^2}} \right)} \right]^{1/2} . \tag{D.2}$$

The nucleation temperature (T_w^{2D}) of $2D$ bounces should be found numerically (ref. [107]) however it will be obviously smaller than T_{crit} (of $(0, v_s) \to (v_h, 0)$ phase transition). At this point we can safely ignore the seeded phase transition effects if all of the domain walls annihilate in the interval of temperatures

$$[T_w, T_{Z_2}], \quad T_w < T_{\text{crit}}, \tag{D.3}$$

where T_w is the temperature when the seeded phase transition will be completed and it is obviously less than T_{crit} of EW phase transition. Let us estimate how strong should be the bias ΔV_B between the potential energies of the two minima of Z_2 potential so that all of the walls can disappear. For these estimates it is sufficient to assume that there is order one difference between T_w and T_{Z_2}, which is generically the case. The critical radius (above which) areas with true vacuum will start to expand is roughly

$$R_c \sim \frac{\sigma}{\Delta V_B}, \tag{D.4}$$

where σ is surface energy density of the wall. So the domain walls will exist on the time scale of

$$\Delta t_w \sim \frac{R_c}{u} \sim \frac{\sigma}{u \Delta V_B}, \tag{D.5}$$

where u is velocity of the wall motion. The change of the temperature during the wall annihilation will be roughly

$$\Delta T \sim T_{\text{crit}} H \Delta t_w. \tag{D.6}$$

So that if $\Delta t_w H \ll 1 \Rightarrow \Delta T \ll T_{\text{crit}}$ the wall annihilation happens almost instantaneously. Assuming $\sigma \sim T_{\text{crit}}^3$ and $H \sim \frac{T_{\text{crit}}^2}{M_{\text{pl}}}$ we get

$$\frac{\Delta V}{T_{\text{crit}}^4} \gg \frac{T_{\text{crit}}}{u M_{\text{pl}}}. \tag{D.7}$$

JHEP10(2022)017

Balancing the pressure against the friction forces $\Delta V_B \sim u T_{\rm crit}^4$ we can estimate the velocity and then the condition for the quick wall annihilation becomes

$$\frac{\Delta V_B}{T_{\rm crit}^4} \gg \sqrt{\frac{T_{\rm crit}}{M_{\rm pl}}} \sim 10^{-8}, \tag{D.8}$$

which is not restrictive at all.

JHEP10(2022)017

References

[1] A. Azatov, M. Vanvlasselaer and W. Yin, *Baryogenesis via relativistic bubble walls*, *JHEP* **10** (2021) 043 [arXiv:2106.14913] [INSPIRE].

[2] A. Azatov, M. Vanvlasselaer and W. Yin, *Dark Matter production from relativistic bubble walls*, *JHEP* **03** (2021) 288 [arXiv:2101.05721] [INSPIRE].

[3] I. Baldes, S. Blasi, A. Mariotti, A. Sevrin and K. Turbang, *Baryogenesis via relativistic bubble expansion*, *Phys. Rev. D* **104** (2021) 115029 [arXiv:2106.15602] [INSPIRE].

[4] A.D. Sakharov, *Violation of CP Invariance, C asymmetry, and baryon asymmetry of the universe*, *Pisma Zh. Eksp. Teor. Fiz.* **5** (1967) 32 [INSPIRE].

[5] V.A. Kuzmin, V.A. Rubakov and M.E. Shaposhnikov, *On the Anomalous Electroweak Baryon Number Nonconservation in the Early Universe*, *Phys. Lett. B* **155** (1985) 36 [INSPIRE].

[6] M.E. Shaposhnikov, *Possible Appearance of the Baryon Asymmetry of the Universe in an Electroweak Theory*, *JETP Lett.* **44** (1986) 465 [INSPIRE].

[7] K. Kajantie, M. Laine, K. Rummukainen and M.E. Shaposhnikov, *A Nonperturbative analysis of the finite T phase transition in SU(2) × U(1) electroweak theory*, *Nucl. Phys. B* **493** (1997) 413 [hep-lat/9612006] [INSPIRE].

[8] M. D'Onofrio and K. Rummukainen, *Standard model cross-over on the lattice*, *Phys. Rev. D* **93** (2016) 025003 [arXiv:1508.07161] [INSPIRE].

[9] D.E. Morrissey and M.J. Ramsey-Musolf, *Electroweak baryogenesis*, *New J. Phys.* **14** (2012) 125003 [arXiv:1206.2942] [INSPIRE].

[10] D.N. Schramm, *Phase Transitions and Dark Matter Problems*, *Nucl. Phys. B* **252** (1985) 53 [INSPIRE].

[11] M.J. Baker and J. Kopp, *Dark Matter Decay between Phase Transitions at the Weak Scale*, *Phys. Rev. Lett.* **119** (2017) 061801 [arXiv:1608.07578] [INSPIRE].

[12] M.J. Baker and L. Mittnacht, *Variations on the Vev Flip-Flop: Instantaneous Freeze-out and Decaying Dark Matter*, *JHEP* **05** (2019) 070 [arXiv:1811.03101] [INSPIRE].

[13] L. Heurtier and H. Partouche, *Spontaneous Freeze Out of Dark Matter From an Early Thermal Phase Transition*, *Phys. Rev. D* **101** (2020) 043527 [arXiv:1912.02828] [INSPIRE].

[14] T. Cohen, D.E. Morrissey and A. Pierce, *Changes in Dark Matter Properties After Freeze-Out*, *Phys. Rev. D* **78** (2008) 111701 [arXiv:0808.3994] [INSPIRE].

[15] L. Bian and Y.-L. Tang, *Thermally modified sterile neutrino portal dark matter and gravitational waves from phase transition: The Freeze-in case*, *JHEP* **12** (2018) 006 [arXiv:1810.03172] [INSPIRE].

[16] L. Hui and E.D. Stewart, *Superheavy dark matter from thermal inflation*, *Phys. Rev. D* **60** (1999) 023518 [hep-ph/9812345] [INSPIRE].

[17] D. Chung, A. Long and L.-T. Wang, *Probing the Cosmological Constant and Phase Transitions with Dark Matter*, *Phys. Rev. D* **84** (2011) 043523 [arXiv:1104.5034] [INSPIRE].

[18] D.J.H. Chung and A.J. Long, *Cosmological Constant, Dark Matter, and Electroweak Phase Transition*, *Phys. Rev. D* **84** (2011) 103513 [arXiv:1108.5193] [INSPIRE].

[19] T. Hambye, A. Strumia and D. Teresi, *Super-cool Dark Matter*, *JHEP* **08** (2018) 188 [arXiv:1805.01473] [INSPIRE].

[20] I. Baldes, Y. Gouttenoire and F. Sala, *String Fragmentation in Supercooled Confinement and Implications for Dark Matter*, *JHEP* **04** (2021) 278 [arXiv:2007.08440] [INSPIRE].

[21] J. Shelton and K.M. Zurek, *Darkogenesis: A baryon asymmetry from the dark matter sector*, *Phys. Rev. D* **82** (2010) 123512 [arXiv:1008.1997] [INSPIRE].

[22] K. Petraki, M. Trodden and R.R. Volkas, *Visible and dark matter from a first-order phase transition in a baryon-symmetric universe*, *JCAP* **02** (2012) 044 [arXiv:1111.4786] [INSPIRE].

[23] I. Baldes, *Gravitational waves from the asymmetric-dark-matter generating phase transition*, *JCAP* **05** (2017) 028 [arXiv:1702.02117] [INSPIRE].

[24] E. Hall, T. Konstandin, R. McGehee and H. Murayama, *Asymmetric Matters from a Dark First-Order Phase Transition*, arXiv:1911.12342 [INSPIRE].

[25] A. Falkowski and J.M. No, *Non-thermal Dark Matter Production from the Electroweak Phase Transition: Multi-TeV WIMPs and 'Baby-Zillas'*, *JHEP* **02** (2013) 034 [arXiv:1211.5615] [INSPIRE].

[26] M.J. Baker, J. Kopp and A.J. Long, *Filtered Dark Matter at a First Order Phase Transition*, *Phys. Rev. Lett.* **125** (2020) 151102 [arXiv:1912.02830] [INSPIRE].

[27] D. Chway, T.H. Jung and C.S. Shin, *Dark matter filtering-out effect during a first-order phase transition*, *Phys. Rev. D* **101** (2020) 095019 [arXiv:1912.04238] [INSPIRE].

[28] D. Marfatia and P.-Y. Tseng, *Gravitational wave signals of dark matter freeze-out*, *JHEP* **02** (2021) 022 [arXiv:2006.07313] [INSPIRE].

[29] S. Ramazanov, E. Babichev, D. Gorbunov and A. Vikman, *Beyond freeze-in: Dark matter via inverse phase transition and gravitational wave signal*, *Phys. Rev. D* **105** (2022) 063530 [arXiv:2104.13722] [INSPIRE].

[30] E. Babichev, D. Gorbunov, S. Ramazanov and A. Vikman, *Gravitational shine of dark domain walls*, *JCAP* **04** (2022) 028 [arXiv:2112.12608] [INSPIRE].

[31] A. Azatov and M. Vanvlasselaer, *Bubble wall velocity: heavy physics effects*, *JCAP* **01** (2021) 058 [arXiv:2010.02590] [INSPIRE].

[32] A. Katz and A. Riotto, *Baryogenesis and Gravitational Waves from Runaway Bubble Collisions*, *JCAP* **11** (2016) 011 [arXiv:1608.00583] [INSPIRE].

[33] P. Baratella, A. Pomarol and F. Rompineve, *The Supercooled Universe*, *JHEP* **03** (2019) 100 [arXiv:1812.06996] [INSPIRE].

[34] L. Delle Rose, G. Panico, M. Redi and A. Tesi, *Gravitational Waves from Supercool Axions*, *JHEP* **04** (2020) 025 [arXiv:1912.06139] [INSPIRE].

JHEP10(2022)017

[35] N. Craig, N. Levi, A. Mariotti and D. Redigolo, *Ripples in Spacetime from Broken Supersymmetry*, *JHEP* **21** (2020) 184 [arXiv:2011.13949] [INSPIRE].

[36] J. Ellis, M. Lewicki, J.M. No and V. Vaskonen, *Gravitational wave energy budget in strongly supercooled phase transitions*, *JCAP* **06** (2019) 024 [arXiv:1903.09642] [INSPIRE].

[37] A. Azatov and M. Vanvlasselaer, *Phase transitions in perturbative walking dynamics*, *JHEP* **09** (2020) 085 [arXiv:2003.10265] [INSPIRE].

[38] J.R. Espinosa and M. Quirós, *Novel Effects in Electroweak Breaking from a Hidden Sector*, *Phys. Rev. D* **76** (2007) 076004 [hep-ph/0701145] [INSPIRE].

[39] A. Noble and M. Perelstein, *Higgs self-coupling as a probe of electroweak phase transition*, *Phys. Rev. D* **78** (2008) 063518 [arXiv:0711.3018] [INSPIRE].

[40] A. Ashoorioon and T. Konstandin, *Strong electroweak phase transitions without collider traces*, *JHEP* **07** (2009) 086 [arXiv:0904.0353] [INSPIRE].

[41] P.H. Damgaard, D. O'Connell, T.C. Petersen and A. Tranberg, *Constraints on New Physics from Baryogenesis and Large Hadron Collider Data*, *Phys. Rev. Lett.* **111** (2013) 221804 [arXiv:1305.4362] [INSPIRE].

[42] T. Alanne, K. Tuominen and V. Vaskonen, *Strong phase transition, dark matter and vacuum stability from simple hidden sectors*, *Nucl. Phys. B* **889** (2014) 692 [arXiv:1407.0688] [INSPIRE].

[43] P. Huang, A.J. Long and L.-T. Wang, *Probing the Electroweak Phase Transition with Higgs Factories and Gravitational Waves*, *Phys. Rev. D* **94** (2016) 075008 [arXiv:1608.06619] [INSPIRE].

[44] A. Beniwal, M. Lewicki, J.D. Wells, M. White and A.G. Williams, *Gravitational wave, collider and dark matter signals from a scalar singlet electroweak baryogenesis*, *JHEP* **08** (2017) 108 [arXiv:1702.06124] [INSPIRE].

[45] V. Barger, P. Langacker, M. McCaskey, M.J. Ramsey-Musolf and G. Shaughnessy, *LHC Phenomenology of an Extended Standard Model with a Real Scalar Singlet*, *Phys. Rev. D* **77** (2008) 035005 [arXiv:0706.4311] [INSPIRE].

[46] J.R. Espinosa, T. Konstandin and F. Riva, *Strong Electroweak Phase Transitions in the Standard Model with a Singlet*, *Nucl. Phys. B* **854** (2012) 592 [arXiv:1107.5441] [INSPIRE].

[47] J. Kozaczuk, M.J. Ramsey-Musolf and J. Shelton, *Exotic Higgs boson decays and the electroweak phase transition*, *Phys. Rev. D* **101** (2020) 115035 [arXiv:1911.10210] [INSPIRE].

[48] Z. Wang et al., *Study of Electroweak Phase Transition in Exotic Higgs Decays at the CEPC*, in *2022 Snowmass Summer Study*, (2022) [arXiv:2203.10184] [INSPIRE].

[49] G. Kurup and M. Perelstein, *Dynamics of Electroweak Phase Transition In Singlet-Scalar Extension of the Standard Model*, *Phys. Rev. D* **96** (2017) 015036 [arXiv:1704.03381] [INSPIRE].

[50] Z. Kang, P. Ko and T. Matsui, *Strong first order EWPT & strong gravitational waves in Z_3-symmetric singlet scalar extension*, *JHEP* **02** (2018) 115 [arXiv:1706.09721] [INSPIRE].

[51] L. Niemi, P. Schicho and T.V.I. Tenkanen, *Singlet-assisted electroweak phase transition at two loops*, *Phys. Rev. D* **103** (2021) 115035 [arXiv:2103.07467] [INSPIRE].

[52] B. Gripaios, A. Pomarol, F. Riva and J. Serra, *Beyond the Minimal Composite Higgs Model*, *JHEP* **04** (2009) 070 [arXiv:0902.1483] [INSPIRE].

[53] J.R. Espinosa, B. Gripaios, T. Konstandin and F. Riva, *Electroweak Baryogenesis in Non-minimal Composite Higgs Models*, *JCAP* **01** (2012) 012 [arXiv:1110.2876] [INSPIRE].

JHEP10(2022)017

[54] L. Bian, Y. Wu and K.-P. Xie, *Electroweak phase transition with composite Higgs models: calculability, gravitational waves and collider searches*, *JHEP* **12** (2019) 028 [arXiv:1909.02014] [INSPIRE].

[55] S. De Curtis, L. Delle Rose and G. Panico, *Composite Dynamics in the Early Universe*, *JHEP* **12** (2019) 149 [arXiv:1909.07894] [INSPIRE].

[56] CMS collaboration, *A measurement of the Higgs boson mass in the diphoton decay channel*, *Phys. Lett. B* **805** (2020) 135425 [arXiv:2002.06398] [INSPIRE].

[57] E.J. Weinberg, *Radiative corrections as the origin of spontaneous symmetry breaking*, Ph.D. thesis, Harvard U., 1973. hep-th/0507214 [INSPIRE].

[58] C. Delaunay, C. Grojean and J.D. Wells, *Dynamics of Non-renormalizable Electroweak Symmetry Breaking*, *JHEP* **04** (2008) 029 [arXiv:0711.2511] [INSPIRE].

[59] M.B. Einhorn and D.R.T. Jones, *A new renormalization group approach to multiscale problems*, *Nucl. Phys. B* **230** (1984) 261 [INSPIRE].

[60] D. Curtin, P. Meade and H. Ramani, *Thermal Resummation and Phase Transitions*, *Eur. Phys. J. C* **78** (2018) 787 [arXiv:1612.00466] [INSPIRE].

[61] M. Quirós, *Finite temperature field theory and phase transitions*, in *ICTP Summer School in High-Energy Physics and Cosmology*, (1999), pp. 187–259 [hep-ph/9901312] [INSPIRE].

[62] P. Schicho, T.V.I. Tenkanen and G. White, *Combining thermal resummation and gauge invariance for electroweak phase transition*, arXiv:2203.04284 [INSPIRE].

[63] P.M. Schicho, T.V.I. Tenkanen and J. Österman, *Robust approach to thermal resummation: Standard Model meets a singlet*, *JHEP* **06** (2021) 130 [arXiv:2102.11145] [INSPIRE].

[64] S.R. Coleman, *The Fate of the False Vacuum. 1. Semiclassical Theory*, *Phys. Rev. D* **15** (1977) 2929 [*Erratum ibid.* **16** (1977) 1248] [INSPIRE].

[65] A.D. Linde, *Fate of the False Vacuum at Finite Temperature: Theory and Applications*, *Phys. Lett. B* **100** (1981) 37 [INSPIRE].

[66] A.D. Linde, *Decay of the False Vacuum at Finite Temperature*, *Nucl. Phys. B* **216** (1983) 421 [*Erratum ibid.* **223** (1983) 544] [INSPIRE].

[67] A.H. Guth and S.H.H. Tye, *Phase Transitions and Magnetic Monopole Production in the Very Early Universe*, *Phys. Rev. Lett.* **44** (1980) 631 [*Erratum ibid.* **44** (1980) 963] [INSPIRE].

[68] A.H. Guth and E.J. Weinberg, *Cosmological Consequences of a First Order Phase Transition in the SU(5) Grand Unified Model*, *Phys. Rev. D* **23** (1981) 876 [INSPIRE].

[69] D. Bödeker and G.D. Moore, *Can electroweak bubble walls run away?*, *JCAP* **05** (2009) 009 [arXiv:0903.4099] [INSPIRE].

[70] M. Dine, R.G. Leigh, P.Y. Huet, A.D. Linde and D.A. Linde, *Towards the theory of the electroweak phase transition*, *Phys. Rev. D* **46** (1992) 550 [hep-ph/9203203] [INSPIRE].

[71] D. Bödeker and G.D. Moore, *Electroweak Bubble Wall Speed Limit*, *JCAP* **05** (2017) 025 [arXiv:1703.08215] [INSPIRE].

[72] Y. Gouttenoire, R. Jinno and F. Sala, *Friction pressure on relativistic bubble walls*, *JHEP* **05** (2022) 004 [arXiv:2112.07686] [INSPIRE].

[73] S. Höche, J. Kozaczuk, A.J. Long, J. Turner and Y. Wang, *Towards an all-orders calculation of the electroweak bubble wall velocity*, *JCAP* **03** (2021) 009 [arXiv:2007.10343] [INSPIRE].

[74] J.M. Cline and K. Kainulainen, *Electroweak baryogenesis and dark matter from a singlet Higgs*, *JCAP* **01** (2013) 012 [arXiv:1210.4196] [INSPIRE].

JHEP10(2022)017

[75] D. Curtin, P. Meade and C.-T. Yu, *Testing Electroweak Baryogenesis with Future Colliders*, *JHEP* **11** (2014) 127 [arXiv:1409.0005] [INSPIRE].

[76] V. Vaskonen, *Electroweak baryogenesis and gravitational waves from a real scalar singlet*, *Phys. Rev. D* **95** (2017) 123515 [arXiv:1611.02073] [INSPIRE].

[77] D. Buttazzo, F. Sala and A. Tesi, *Singlet-like Higgs bosons at present and future colliders*, *JHEP* **11** (2015) 158 [arXiv:1505.05488] [INSPIRE].

[78] S. Profumo, M.J. Ramsey-Musolf and G. Shaughnessy, *Singlet Higgs phenomenology and the electroweak phase transition*, *JHEP* **08** (2007) 010 [arXiv:0705.2425] [INSPIRE].

[79] H.H. Patel and M.J. Ramsey-Musolf, *Stepping Into Electroweak Symmetry Breaking: Phase Transitions and Higgs Phenomenology*, *Phys. Rev. D* **88** (2013) 035013 [arXiv:1212.5652] [INSPIRE].

[80] W. Huang, Z. Kang, J. Shu, P. Wu and J.M. Yang, *New insights in the electroweak phase transition in the NMSSM*, *Phys. Rev. D* **91** (2015) 025006 [arXiv:1405.1152] [INSPIRE].

[81] M. Jiang, L. Bian, W. Huang and J. Shu, *Impact of a complex singlet: Electroweak baryogenesis and dark matter*, *Phys. Rev. D* **93** (2016) 065032 [arXiv:1502.07574] [INSPIRE].

[82] C.-W. Chiang, M.J. Ramsey-Musolf and E. Senaha, *Standard Model with a Complex Scalar Singlet: Cosmological Implications and Theoretical Considerations*, *Phys. Rev. D* **97** (2018) 015005 [arXiv:1707.09960] [INSPIRE].

[83] V. Guada, M. Nemevšek and M. Pintar, *FindBounce: Package for multi-field bounce actions*, *Comput. Phys. Commun.* **256** (2020) 107480 [arXiv:2002.00881] [INSPIRE].

[84] R. Barbieri and G.F. Giudice, *Upper Bounds on Supersymmetric Particle Masses*, *Nucl. Phys. B* **306** (1988) 63 [INSPIRE].

[85] J. Ellis, M. Lewicki and J.M. No, *On the Maximal Strength of a First-Order Electroweak Phase Transition and its Gravitational Wave Signal*, *JCAP* **04** (2019) 003 [arXiv:1809.08242] [INSPIRE].

[86] K. Enqvist, J. Ignatius, K. Kajantie and K. Rummukainen, *Nucleation and bubble growth in a first order cosmological electroweak phase transition*, *Phys. Rev. D* **45** (1992) 3415 [INSPIRE].

[87] I. Baldes, Y. Gouttenoire, F. Sala and G. Servant, *Supercool composite Dark Matter beyond 100 TeV*, *JHEP* **07** (2022) 084 [arXiv:2110.13926] [INSPIRE].

[88] LISA collaboration, *Laser Interferometer Space Antenna*, arXiv:1702.00786 [INSPIRE].

[89] C. Caprini et al., *Detecting gravitational waves from cosmological phase transitions with LISA: an update*, *JCAP* **03** (2020) 024 [arXiv:1910.13125] [INSPIRE].

[90] C. Caprini et al., *Science with the space-based interferometer eLISA. II: Gravitational waves from cosmological phase transitions*, *JCAP* **04** (2016) 001 [arXiv:1512.06239] [INSPIRE].

[91] B. Von Harling, A. Pomarol, O. Pujolàs and F. Rompineve, *Peccei-Quinn Phase Transition at LIGO*, *JHEP* **04** (2020) 195 [arXiv:1912.07587] [INSPIRE].

[92] V. Brdar, A.J. Helmboldt and J. Kubo, *Gravitational Waves from First-Order Phase Transitions: LIGO as a Window to Unexplored Seesaw Scales*, *JCAP* **02** (2019) 021 [arXiv:1810.12306] [INSPIRE].

[93] V. Corbin and N.J. Cornish, *Detecting the cosmic gravitational wave background with the big bang observer*, *Class. Quant. Grav.* **23** (2006) 2435 [gr-qc/0512039] [INSPIRE].

[94] J. Crowder and N.J. Cornish, *Beyond LISA: Exploring future gravitational wave missions*, *Phys. Rev. D* **72** (2005) 083005 [gr-qc/0506015] [INSPIRE].

JHEP10(2022)017

[95] N. Seto, S. Kawamura and T. Nakamura, *Possibility of direct measurement of the acceleration of the universe using 0.1-Hz band laser interferometer gravitational wave antenna in space*, *Phys. Rev. Lett.* **87** (2001) 221103 [astro-ph/0108011] [INSPIRE].

[96] K. Yagi and N. Seto, *Detector configuration of DECIGO/BBO and identification of cosmological neutron-star binaries*, *Phys. Rev. D* **83** (2011) 044011 [*Erratum ibid.* **95** (2017) 109901] [arXiv:1101.3940] [INSPIRE].

[97] S. Isoyama, H. Nakano and T. Nakamura, *Multiband Gravitational-Wave Astronomy: Observing binary inspirals with a decihertz detector, B-DECIGO*, *PTEP* **2018** (2018) 073E01 [arXiv:1802.06977] [INSPIRE].

[98] S. Hild et al., *Sensitivity Studies for Third-Generation Gravitational Wave Observatories*, *Class. Quant. Grav.* **28** (2011) 094013 [arXiv:1012.0908] [INSPIRE].

[99] B. Sathyaprakash et al., *Scientific Objectives of Einstein Telescope*, *Class. Quant. Grav.* **29** (2012) 124013 [*Erratum ibid.* **30** (2013) 079501] [arXiv:1206.0331] [INSPIRE].

[100] M. Maggiore et al., *Science Case for the Einstein Telescope*, *JCAP* **03** (2020) 050 [arXiv:1912.02622] [INSPIRE].

[101] L. Badurina et al., *AION: An Atom Interferometer Observatory and Network*, *JCAP* **05** (2020) 011 [arXiv:1911.11755] [INSPIRE].

[102] AEDGE collaboration, *AEDGE: Atomic Experiment for Dark Matter and Gravity Exploration in Space*, *EPJ Quant. Technol.* **7** (2020) 6 [arXiv:1908.00802] [INSPIRE].

[103] D. Cutting, M. Hindmarsh and D.J. Weir, *Gravitational waves from vacuum first-order phase transitions: from the envelope to the lattice*, *Phys. Rev. D* **97** (2018) 123513 [arXiv:1802.05712] [INSPIRE].

[104] J.R. Espinosa, T. Konstandin, J.M. No and G. Servant, *Energy Budget of Cosmological First-order Phase Transitions*, *JCAP* **06** (2010) 028 [arXiv:1004.4187] [INSPIRE].

[105] S. Argyropoulos, O. Brandt and U. Haisch, *Collider Searches for Dark Matter through the Higgs Lens*, *Symmetry* **13** (2021) 2406 [arXiv:2109.13597] [INSPIRE].

[106] S. Bruggisser, B. Von Harling, O. Matsedonskyi and G. Servant, *Electroweak Phase Transition and Baryogenesis in Composite Higgs Models*, *JHEP* **12** (2018) 099 [arXiv:1804.07314] [INSPIRE].

[107] S. Blasi and A. Mariotti, *Domain walls seeding the electroweak phase transition*, arXiv:2203.16450 [INSPIRE].

JHEP10(2022)017